

**Experimental and Analytical Study of the
Hydroacoustics of Propellers in Rigid Ducts**

Scott C. Morris

Thomas Mueller

Final Report

Grant No. N00014-04-1-0193

by the

University of Notre Dame

Notre Dame, Indiana

for the

Department of the Navy

Office of Naval Research

Arlington, Virginia

DISTRIBUTION STATEMENT A
Approved for Public Release
Distribution Unlimited

UND-SCM06-0324

July 2006

20060808092

REPORT DOCUMENTATION PAGE

Form Approved
OMB No. 0704-0188

The public reporting burden for this collection of information is estimated to average 1 hour per response, including the time for reviewing instructions, searching existing data sources, gathering and maintaining the data needed, and completing and reviewing the collection of information. Send comments regarding this burden estimate or any other aspect of this collection of information, including suggestions for reducing the burden, to Department of Defense, Washington Headquarters Services, Directorate for Information Operations and Reports (0704-0188), 1215 Jefferson Davis Highway, Suite 1204, Arlington, VA 22202-4302. Respondents should be aware that notwithstanding any other provision of law, no person shall be subject to any penalty for failing to comply with a collection of information if it does not display a currently valid OMB control number.

PLEASE DO NOT RETURN YOUR FORM TO THE ABOVE ADDRESS.

1. REPORT DATE (DD-MM-YYYY) 31-July, 2006	2. REPORT TYPE Final Technical Report	3. DATES COVERED (From - To) 1-Jan, 2004 to 31-Mar, 2006
---	---	--

4. TITLE AND SUBTITLE Experimental and Analytical Study of the Hydroacoustics of Propellers in Rigid Ducts	5a. CONTRACT NUMBER N00014-04-1-0192
	5b. GRANT NUMBER
	5c. PROGRAM ELEMENT NUMBER

6. AUTHOR(S) Morris, Scott C. Mueller, Thomas J.	5d. PROJECT NUMBER
	5e. TASK NUMBER
	5f. WORK UNIT NUMBER

7. PERFORMING ORGANIZATION NAME(S) AND ADDRESS(ES) Department of Aerospace and Mechanical Engineering University of Notre Dame	8. PERFORMING ORGANIZATION REPORT NUMBER UND-SCM06-0324
---	---

9. SPONSORING/MONITORING AGENCY NAME(S) AND ADDRESS(ES) Office of Naval Research Ballston Centre Tower One 800 North Quincy Street Arlington, VA 22217-5660	10. SPONSOR/MONITOR'S ACRONYM(S) ONR
	11. SPONSOR/MONITOR'S REPORT NUMBER(S)

12. DISTRIBUTION/AVAILABILITY STATEMENT
Approved for Public Release; distribution is Unlimited

13. SUPPLEMENTARY NOTES

14. ABSTRACT
This report describes the results of a detailed study of the fluid dynamics and acoustic signature of a rotor operating in a rigid duct. The study focused on the separation of the acoustic source functions and the system response, or transfer function. A new algorithm was developed and quantified to separate these functions from radiated sound measurements. Measurements of the approach flow turbulence and propeller wake turbulence provided insight into the nature of the acoustics sources. It was found that approach flow noise is only responsible for the sound produced at frequencies less than the first blade rate tone. Higher frequencies were dominated by complex rotor self noise that included broad humps in the source spectra at integer multiples of the blade passing frequency.

15. SUBJECT TERMS
shaftless propulsion, ducted propeller, hydroacoustics

16. SECURITY CLASSIFICATION OF:			17. LIMITATION OF ABSTRACT UU	18. NUMBER OF PAGES 60	19a. NAME OF RESPONSIBLE PERSON
a. REPORT U	b. ABSTRACT U	c. THIS PAGE U			19b. TELEPHONE NUMBER (Include area code)

FORWARD

The work reported herein was performed by the Department of Aerospace and Mechanical Engineering, University of Notre Dame, for the U.S. Navy, Office of Naval Research, Arlington, Virginia, under Grant No. N00014-04-1-0193. The program manager was Dr. Ki-Han Kim. Additional support necessary to bring this work to a meaningful conclusion was supplied by the University of Notre Dame. This research was performed between January 1, 2004 and March 31, 2006.

ABSTRACT

A subsonic ducted rotor such as a fan, compressor, or propeller that is operating in a finite length duct generates a complicated acoustic source. The sound producing mechanisms involve interactions between the rotor and the turbulent flow field that result in unsteady forces and dipole sound. In many applications, the spectral character of the sound radiated from the system can be significantly different from that of the acoustic source due to the presence of rigid, non-rigid, and damping surfaces which can act to amplify or attenuate certain frequencies of the source spectra. The radiated sound from these systems depends on the coupling of the distributed sound sources with the acoustic characteristics of the surrounding surfaces. The present document describes experimental and analytical work from a detailed study of the fluid motions and resulting sound sources of a subsonic ducted propeller.

A new method for analyzing measurements of sound radiated from aeroacoustic systems has been developed as part of this project. This method assumed the radiated sound to be a combination of a compact source with a "blocked" transfer function. Experimental results from a single stage low speed rotor operating in a finite length duct provided a database for development and evaluation of the algorithm. The measurements were acquired at various rotor operating points in order to obtain varied sound source characteristics without changing the rigid geometry of the system. Typical agreement in the resolved transfer functions was found to be 0.26 dB.

The effect of mean blade loading, approach turbulence and tip clearance on the sound sources in the ducted rotor was investigated. Radiated acoustic measurements were acquired at a range of speeds and operating points on the characteristic curve of the system. In addition, hot wire anemometry was used to document the salient features of the flow field. It was found that the sound spectra was dominated by tones at multiples of the blade passing frequency at higher flow rates. At lower flow rates, part span stall led to local maxima in the acoustic spectra at non-integer multiples of the blade passing frequency.

CONTENTS

FORWARD	i
ABSTRACT	ii
FIGURES	v
SECTION 1: Introduction	1
1.1 Overview	1
1.2 Aerodynamic Sound	2
SECTION 2: Background	4
2.1 Rotor Acoustics	4
2.1.1 Approach Noise Literature	4
2.1.2 Self Noise Literature	7
2.1.3 Experimental Studies of Rotor Noise	7
2.2 Duct Acoustics	8
2.2.1 Duct Cross-Sectional Eigenfunctions	9
2.2.2 Duct Organ Pipe Modes	11
2.2.3 Analytical Free Space Dipole Green's Function	11
SECTION 3: Experimental Setup	14
3.1 Flow Field Measurements	15
3.2 Microphone Measurements	15
3.3 Experimental Parameters	15
SECTION 4: Blocked Model Calculation of Transfer Function	17
4.1 Blocked Modeling Representation	17
4.2 Fundamental Frequencies of the Ducted Rotor System	19
4.3 Review of Previous Work	20
4.4 Source-Transfer Function Separation Method	22
4.4.1 Aeroacoustic Scaling Model	22
4.4.2 Implementation as a Computer Algorithm	22
4.5 Evaluation of Separation Method	23
4.5.1 Error Analysis of the Algorithm	23
4.5.2 Separation Algorithm Applied to Varied Sound Source Data	26
4.5.3 Separation Algorithm Applied to Varied Transfer Function Data	28
4.6 Summary of Separation Algorithm	29

SECTION 5: Flow Field and Acoustic Source Results	33
5.1 Flow Fields Results	33
5.2 Sound Source Variation with Operating Point	38
5.2.1 Unsteady Force Spectra	38
5.2.2 Sound Source Scaling	40
5.3 Sound Source Results with Downstream Support Struts	40
5.4 Sound Source Variation with Tip Gap	42
 SECTION 6: Conclusions	 45
 APPENDIX A: Evaluation of Blocked Modeling	 47
 APPENDIX B: Nomenclature	 50
 BIBLIOGRAPHY	 54

FIGURES

1.1	Sources of sound on a lifting surface.	3
2.1	Elongation of ingested turbulent structures that is a potential tonal noise source.	6
2.2	Variation of the speed exponent with flow coefficient.	9
2.3	Experimental sound source separation method used in Ganz et al.	10
2.4	Results of sound source separation experiment from Ganz et al.	11
2.5	Illustrations of mode shapes for circular duct acoustic modes; q = number of node circles, p = number of node diameters.	13
3.1	Schematic of experimental model.	14
3.2	Dimensionless rotor characteristic curve. Arrows denote operating conditions where detailed measurements were made.	16
4.1	Measured sound spectra for ducted rotor at three rotational speeds.	20
4.2	Measured sound spectra for ducted rotor at three rotational speeds, frequency normalized as St	21
4.3	Experimental data showing linear fit to $D_{guess}(St)$	24
4.4	Experimental data showing sound source linear scaling after transfer function has been removed.	25
4.5	Example simulated transfer function.	26
4.6	Error for different values of <i>feature size ratio</i> and speed ratio after three iterations.	27
4.7	Measured sound under different loading conditions at 5000 RPM.	28
4.8	Calculated transfer functions for $\phi = 0.17, 0.22, 0.30$ and 0.42	29
4.9	Measured sound at 5000 RPM for varying duct lengths.	30
4.10	Transfer function result for different length ducts.	31
4.11	Sound source spectra at 5000 RPM for varying duct lengths.	32
5.1	Mean and RMS of axial component of velocity in plane $x/R_{tip} = 0.25$ upstream of rotor.	34
5.2	Velocity spectra of approach flow in plane $x/R_{tip} = 0.25$ upstream of rotor.	35
5.3	Phase mean velocity \bar{u}/U_0 measured at $x/R_{tip} = 0.031$	36
5.4	Phase RMS velocity \tilde{u}/U_0 measured at $x/R_{tip} = 0.031$	37
5.5	Autospectral density of axial velocity at $r/R_{tip} = 0.98, x/R_{tip} = 0.0625$	38
5.6	Sound source spectra for rotor at 5000 RPM.	40
5.7	Power law scaling of rotor sound source.	41
5.8	Sound source spectra for rotor at 5000 RPM comparing struts upstream and downstream configurations.	42
5.9	Sound source spectra for rotor at 5000 RPM with varied tip gap. $\phi = 0.30$	43
5.10	Sound source spectra for rotor at 5000 RPM with varied tip gap. $\phi = 0.20$	44

A.1	Plot of $P_{1,1} - P_{2,1} - P_{1,2} + P_{2,2}$	48
A.2	Four combinations of two sound sources and two transfer functions.	49

SECTION 1

Introduction

1.1 Overview

This report describes the results and conclusions of an experimental study of ducted rotor acoustics. The use of a duct in aerial and marine propulsion systems as opposed to an open propeller design affords a number of distinct advantages. For example, the thrust produced for a given rotor diameter can be considerably greater since the exit flow can be accelerated through a discharge nozzle. A ducted rotor design also offers flexibility in marine architecture because it removes the need for a single shafted propeller. Despite the lowered efficiency of ducted propulsion system, these and other advantages have led the U.S. Navy to consider various "shaftless propulsion" configurations for its next generation of submarine vehicles. The intent is for these systems to allow increased payload fraction, reduced construction and operating costs, and enhanced maneuverability.

The acoustic signature for both ducted propulsion systems and traditional, open propellers are both related to force dipoles on the blades due to blade-turbulence interactions. However, the nature of these interactions can be significantly different for the two rotor types. For example, an open propeller operates such that the blade tips (where the relative velocity is maximum), is near the outermost part of the hull boundary layer. In an embedded propulsion system, the hull boundary layer is drawn in to the inlet such that the rotor experiences a strongly distorted approach flow, with duct wall boundary layers that interact with the blade tips.

The propagation of acoustic energy to the far field can be significantly more complex in ducted systems compared to an open propeller. For example, the distribution of acoustic sources is not compact with respect to the duct diameter. Also, reflected waves from the duct ends can lead to standing waves known as organ pipe modes. The coupling of these phenomena with elastic structures further complicates the prediction of far field sound. The duct would most likely have stiffeners, or ribs, that act as local scattering points for structure borne sound.

The research conducted in this project was part of a larger program funded by the Office of Naval Research (ONR). Specifically, the recent HIDO model studies have investigated ducted rotor acoustics in geometries that are notionally similar to submarine applications. These studies found a number of important similarities among these systems, and have identified a number of important challenges for the understanding and a-priori prediction of the acoustic signature. The present work both supports and extends the results from these prior studies. Specifically, the motivation for the present work was:

1. To study the sound generated from a highly configurable and simple ducted rotor system,
2. To separate and identify the acoustics sources and the acoustic transfer function,
3. To use the variability of the system to isolate and investigate different source mechanisms (turbulent ingestion noise, self noise, tip noise, etc.),
4. To obtain detailed measurements of the unsteady fluid motions upstream and downstream of the rotor in order to understand the nature of the force dipoles, and
5. To provide source field information as a baseline case for ongoing research using thin, elastic shells.

The main objectives of this project were met, and the basic results of the study are contained herein. Additional measurements are presently being acquired, and additional processing and analysis of existing and new data is underway. The authors can be contacted for further information beyond what is contained in this final report.

1.2 Aerodynamic Sound

Aerodynamic sound in a subsonic rotor is primarily generated by unsteady forces on rigid surfaces, that is, turbulent flows interacting with the rotor blades. Goldstein[1] provides a derivation of Lighthill's acoustic analogy, one of the fundamental equations of aeroacoustics. The equation is derived from the Navier-Stokes equations and forms the basis of many aeroacoustic theories,

$$\rho' = \frac{1}{c_0^2} \int_{-T}^T \int_{v(\tau)} \frac{\partial^2 G}{\partial y_i \partial y_j} T_{ij} dy d\tau + \frac{1}{c_0^2} \int_{-T}^T \int_{S(\tau)} \frac{\partial G}{\partial y_i} f_i dS(\mathbf{y}) d\tau + \frac{1}{c_0^2} \int_{-T}^T \int_{S(\tau)} \rho_0 V_n \frac{\partial G}{\partial \tau} dS(\mathbf{y}) d\tau. \quad (1.1)$$

The equation expresses the unsteady fluid density ρ' in terms of a region of fluid $v(\tau)$, with surfaces $S(\tau)$, fluid stresses T_{ij} and surface forces f_i . The first term accounts for sound generated in a volume of fluid and is important for high speed jet noise and other systems with high fluid stresses, but is negligible for low mach number turbomachinery. The third term is important in systems with mass flux, or where significant fluid displacement occurs due to moving surfaces. For the present work the middle term in Equation 1.1 is dominant; the sources of aerodynamic sound are primarily due to unsteady fluid forcing on the rotor blades. To summarize, the following sources of noise are considered negligible or not relevant to the current work: Jet noise, noise related to shock waves or other high mach number effects, rotation (Gutin) noise due to steady thrust and torque and monopole or source noise due to thickness effects of the blades.

There are many different mechanisms which can lead to unsteady fluid forces on the rotor blades and some of these are illustrated in Figure 1.1. These mechanisms of rotor noise can be divided into two categories, *approach noise* and *self noise*. Approach noise is any sound that is dependent on the flow ingested by the rotor, while self noise is sound that is generated by the rotor independent of the approach flow properties. These two categories are further broken down in the following lists adapted from Blake[2].

Important causes of approach noise are:

1. Rotor blades ingesting small-scale turbulence,
2. Inlet disturbances and other large-scale turbulence, and
3. Rotor blade interaction with duct or casing boundary layers.

Important causes of self-noise on rotor blades are:

4. Blade-blade tip vortex interaction,
5. Turbulence in the rotor blade boundary layer convecting past trailing edges,
6. Laminar flow separation and lift breakdown causing unsteady pressure, and
7. Laminar vortex development in the trailing wake.

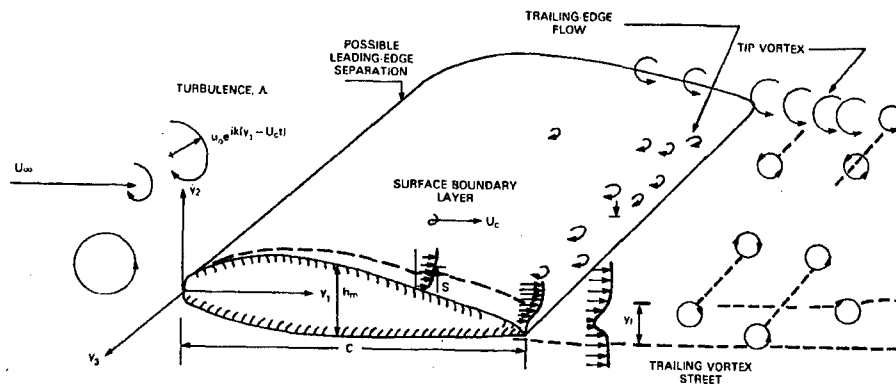


Figure 1.1. Sources of sound on a lifting surface. Figure adapted from Blake[2].

The focus of the present research was on the relative importance of these different sound sources and the connection between the sound producing mechanisms and the fluid motions that cause them, as well as the acoustic transfer function between the sound sources and the far field. An experimental facility was developed with highly configurable boundary conditions that was used to study the sources of noise found in the above list. Experimental measurements were used to determine the effectiveness of blocked modeling, and to develop an algorithm to separate the rotor sound sources from the acoustic transfer function[3]. The rotor was also studied under a range of mean blade loading conditions, and different sound sources were found to be dominant at different operating points[4]. These and other results will be presented in the following sections.

Section 2 will review some literature that is particularly relevant to the present work. The experimental setup that has been designed and constructed for this research will be described in Section 3. Section 4 will describe the blocked model data processing technique that has been developed to separate the measured sound into a blocked source spectra and a blocked transfer function spectra. Section 5 will present the results from a study of the rotor system under a range of operating conditions. Section 6 will summarize the major findings of this study.

SECTION 2

Background

The two subsections that follow describe rotor acoustics and duct acoustics, respectively. The literature that is discussed is a sampling of the most current and most relevant work that has been done in the field, and is not an exhaustive review. Both fields are well developed enough that extensive literature is available, as well as a number of excellent review articles[5][6].

2.1 Rotor Acoustics

A report by Huff[7] discusses the status of fan noise modeling as of 1997 and discusses deficiencies in the knowledge base. The report reviews both analytical and computational aeroacoustic (CAA) methods, focusing on the predictive capabilities of the current methods and the underlying fluid mechanics. Huff concludes that it is still unclear what fan noise sources are most important to model in order to predict fan noise, but points out that current models predict tonal sound more accurately than broadband. Huff identifies a particular deficiency in rotor-stator interaction noise, and the understanding of the fluid flow in this region. Huff believes that current duct propagation and radiation models effectively predict the far field sound when the source distribution inside the duct can be accurately provided.

The following subsections will review some of the same papers discussed in the NASA report, as well as several others. Particular attention will be paid to work that considers predictive methods for realistic systems. The first subsection discusses literature related specifically to approach noise, while the second subsection covers self noise. The third subsection describes the findings of some experimental studies that are particularly relevant to the current study.

2.1.1 Approach Noise Literature

Tonal noise due to rotor-stator interaction

Fan tone noise predominantly occurs at integer multiples of the blade passing frequency ($BPF=B\Omega$). An upstream guide vane or support strut can cause a velocity deficit that is ingested into the rotor, and these inflow distortions occur at regular intervals in the fan rotation. The rotor perceives this velocity deficit as a change angle of attack and a corresponding change in lift force occurs. A method developed by Kobayashi[8] and evaluated in detail by Kobayashi and Groeneweg[9] models a rotor as a rotating cascade of blades and

predicts the tonal response due to any inflow distortion that can be described in a Fourier-Bessel decomposition. Tonal noise was found to be dependent on the width of a periodic inflow distortion, such that for a single gaussian inflow distortion, the most sound was generated when the distortion half-width was about .015 radians for a rotor with 15 blades.

A direct method for calculating sound due to a three-dimensional gust interacting with a cascade of airfoils was developed by Atassi et al.[10]. Euler's equations were linearized about the mean flow and the fluctuating portion of the flow leads to unsteady pressures and radiated sound. The method was extended by Elhadidi and Atassi[11] to consider the wake of a rotor impinging on an annular stator, and a variety of stator configurations were examined including cases of lean and sweep in order to reduce tonal noise.

Broadband inflow noise due to ingested small-scale turbulence

The inflow into any realistic turbomachine is turbulent, with a wide range of length scales. When a turbulent gust is ingested into the rotor it causes a change in loading on the rotor blades. A turbulent structure is considered of small scale if only one blade interacts with it as it passes through the rotor. Since the turbulent motions are of many different sizes, the noise generated is broadband in nature. The simplified system of an airfoil in steady flow experiencing a transverse gust was first solved by Sears[12]. A Sears function approach to predict inflow noise due to small-scale turbulence was derived by Blake[2] and others as,

$$\mathcal{D}_s(f) = B \frac{\pi^2}{3} [\rho(\Omega R_t)^2]^2 (C R_t)^2 \frac{\tilde{u}}{(\Omega R_t)^2} \left| S_e \left(\frac{\pi f C}{U_t} \right) \right|^2 \frac{2\Lambda}{R_t} \cos^2 \gamma \frac{1}{U_t} \Phi \left(\frac{2\pi f}{U_t} \right), \quad (2.1)$$

where Φ is the wave number spectra of the approach turbulence. This equation was derived from a weighted integral of unsteady forces over the radius of the blade and assumes isentropic turbulence and compact sources. A study by Lynch et al.[13] provides expressions for relating point measurements of the flow field to the correlation length scales that are required for this kind of acoustic model.

An experimental study by Scharpf and Mueller[14] considered the sound radiated by a four-bladed propeller subjected to grid-generated turbulence. The turbulence levels were varied and far field microphone measurements were acquired, and hot wires were used to measure velocity coherence in the rotor wake. It was found that increasing the turbulence level by 1% resulted in a 2 dB increase in the overall broadband sound levels. The same four-bladed propeller was studied by Subraminian[15] using computational methods. It was found that radiated tonal noise could be predicted with reasonable accuracy in both magnitude and directivity.

Wojno et al.[16] used a semi-empirical model for the ingested turbulence and strip-theory to predict the radiated sound from the same 10-bladed propeller used in the current research. Predictions of the broadband sound were obtained between 1 and 3 BPF.

Tonal noise due to large-scale turbulence

Tonal noise can be due to large scale turbulent motions, which may have a different mean velocity or a rotating motion that causes a variation in the approach flow to the rotor.

As a basic model for turbulence with an axial correlation length (2Λ) that is greater than the spacing of the blades, Blake suggests using the following expression for the unsteady thrust,

$$\mathcal{D}_t(f, \Delta f) = \frac{4\pi^3}{3} \frac{\Delta f}{\Omega} \rho^2 U_0^4 R_t^4 \left(\frac{C}{R_t}\right)^2 \left(\frac{\Omega R_t}{U_0}\right) \frac{\overline{u_2^2}}{U_0^2} \left(\frac{2\Lambda}{R_t}\right) \frac{\Lambda/\pi R_t}{1 + (\Lambda m B/R_t)^2} \frac{|A_s(2\pi f/\Omega)|^2}{1 + \pi m B C/R_t} \quad (2.2)$$

with the acceptance function $A_s(k_\theta b) = \sum_{s=0}^{B-1} e^{ik_\theta s b}$.

An extensive experimental study of rotor aerodynamics and radiated sound was conducted by Trunzo et al.[17]. A major source of tonal sound was determined to be elongated turbulent eddies ingested from the free stream, as shown in Figure 2.1. As turbulent structures with size on the order of the inlet diameter were ingested, the streamlines caused them to be compressed in the plane of the rotor and elongated, such that several rotor blades interacted with the same structure, producing correlated sound at multiples of BPF.

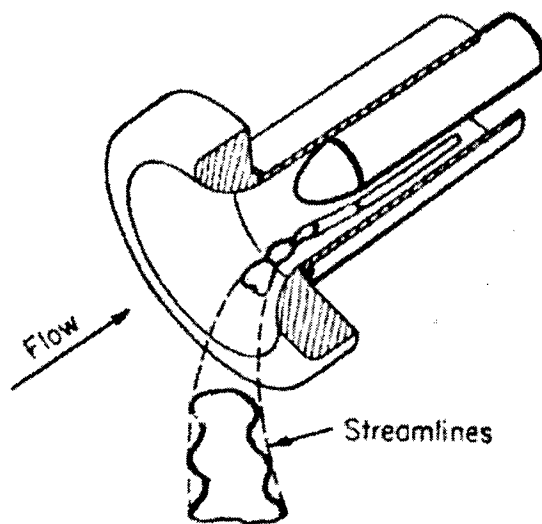


Figure 2.1. Elongation of ingested turbulent structures that is a potential tonal noise source.
Figure from Trunzo et al.[17]

Boundary layer-rotor tip interaction noise

Moissev et al.[18] considered an annular ducted rotor ingesting various types of grid-generated and duct wall boundary layer turbulence. Correlation length scales of the various turbulence cases were measured in axial and tangential directions. Far field sound directivity at BPF = 1 was measured and found to be nearly featureless between zero and 90 degrees. Results of far field sound spectra were presented for cases with a 10 bladed and a 17 bladed rotor with and without grid generated turbulence and with a several kinds of boundary layers. Addition of a grid was found to reduce the tonal sound generated at multiples of

BPF. The authors believe this effect was likely due to breakup of axial large scale motions. The effect is largely to reduce the 2nd and higher multiple of BPF, with BPF=1 mostly unchanged. The 10 bladed rotor was found to be louder than the 17 blade rotor at identical loading conditions, an effect attributed to increased per-blade loading. A case with a fully developed boundary layer inflow was found to be the loudest for both rotors, and up to 10 dB louder for the 10 bladed rotor. Three different flow coefficients were also tested, and the increasing flow coefficient led to louder broadband sound. The authors conclude that most of the sound is generated by the hub and tip regions of the rotor and due to the ingested boundary layer.

2.1.2 Self Noise Literature

The turbulent motions in the rotor blade boundary layers create unsteady forces on the rotor blade as they convect over the trailing edge, and these fluid motions are difficult to describe analytically. Consequently far fewer studies have treated self noise.

A database of acoustic measurements was made by Brooks and Marcolini[19], who made acoustic measurements of a number of cambered and symmetric airfoils under a wide range of flow conditions. This database was later extended into an empirical self-noise prediction code[20]. The self-noise code was used by Glegg and Jochault[21] to predict self-noise from a ducted fan. Their approach was to take the Green's function for a rigid circular duct as provided by Goldstein[1], and use it to simplify the acoustic analogy, given as Equation 1.1. The self-noise code for a rigid airfoil was utilized and appropriate considerations for rotating sources and duct mode coupling was made. The results of the paper were broadband self-noise sound predictions for a rotor in a rigid duct as a function of duct flow rate, blade twist and other parameters.

Some other examples of recent self noise studies include tip vortex noise[22] and blade vortex shedding noise[23].

2.1.3 Experimental Studies of Rotor Noise

Longhouse[24] considered a .365 m diameter, 8 bladed axial flow fan in duct with a blower in a configuration that was similar to the experimental setup used in the present research. The test varied many experimental parameters, however only total sound power was considered, instead of a power spectrum. The following is a summary of conclusions related to the different experimental parameters that were considered:

Flow Coefficient Sound generally increased for lower flow rates and decreased with higher flow rates. The curve is not completely monotonic, with some features at flow rates lower than the design flow rate.

Tip Clearance Longhouse concludes that noise at low flow rates was related to the interaction of the rotor tip with the tip clearance vortex. Reducing the tip clearance from the design for automotive purposes did little to the sound field until the minimum operational clearance was reached, and approximately 15 dB noise reduction was found for low flow coefficients.

Blade Pitch Angle Changing the blade angle was found to essentially just change the loading, and similar results were drawn as with changes to flow coefficient.

Inflow Disturbances Cylinders were placed upstream of the rotor in order to create cyclical inflow disturbances. Sound was lowest with zero upstream rods, increasing with four and eight, but decreasing again with 12. An analytical model was used to predict the sound power due to the various number of upstream cylinders and good agreement was found. The sound was found to increase at higher flow rates, leading to a minimum sound power at a flow rate between minimum and maximum for the case with upstream rods.

Longhouse described the total radiated sound pressure in terms of the scaling relation, first presented by Mellin[25],

$$\text{SPL} \propto V_{tip}^{\chi} (2R_d)^2, \quad (2.3)$$

and the exponent χ was plotted for various flow rates, as shown in Figure 2.2. In the case of zero upstream disturbances a minimum value of around 3 was found for flow rates near the design point, and at low flow rates of a value of about 5 was found. An analytical prediction of 4.86 from Mellin[25] was noted. Adding rods makes the exponent χ nearly independent of flow rate, as presumably in the case with upstream rods the sound was dominated by the approach flow. Another important conclusion was that the at low flow rates loading noise was most important, at high flow rates noise due to upstream rods was dominant and both were important around the design condition. Longhouse concludes that minimum noise and maximum efficiency operating points were unrelated.

Ganz et al.[26], in a more recent study, considered a fan rig based on a jet engine, operating with a fan, and with removable stator and inlet guide vanes. Their work assumes that the different sound sources described in Section 1 are largely uncoupled, that is, they act independently, and careful experimental work can reduce level of some of the sources in order to identify the separate contributions to the total sound spectrum. Ganz et al. measured the radiated sound from a rotor stage operated with and without a downstream stator, with the boundary layer removed and with different kinds of ingested turbulence. By operating without the stator and the boundary layer removed by suction, an estimate for the noise due only to the rotor was obtained. By subtracting this radiated sound pressure from that obtained when the stator or boundary layer were added, the respective contributions to the total radiated sound was estimated. This process is illustrated in Figure 2.3, and a typical example of the results is shown in Figure 2.4.

2.2 Duct Acoustics

Rotating machinery typically operates in a finite length duct or other geometry. The sound generated by the sources is reflected and scattered by the geometry before being radiated to the far field. Additionally, there are effects due to the distribution of sources within the duct, duct organ-pipe modes, cut-on frequencies and the location of the rotor within duct. An extensive review is provided by Doak[6]. These effects significantly alter the propagation of the sound produced by the rotor. and strongly influence the spectral

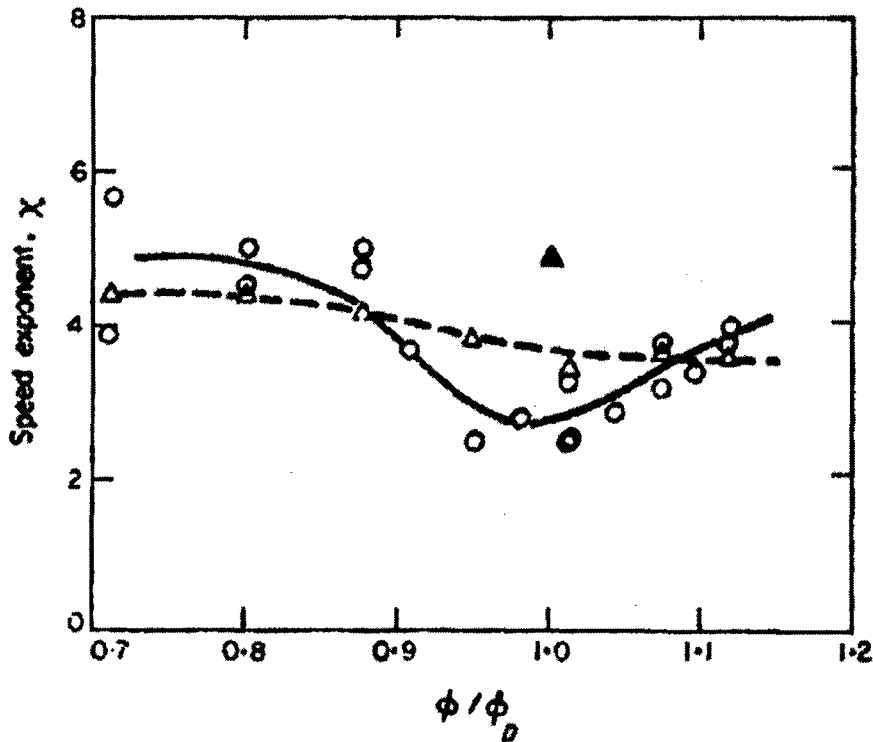


Figure 2.2. Variation of the speed exponent with flow coefficient. Experimental: \circ —, no rods (on axis); \circ —, no rods (90°); Δ — — —, 8 rods (on axis). Analytical prediction: \blacktriangle , 8 rods (on axis). ϕ_D , design flow rate. Figure from Longhouse[24].

character of the sound as perceived by an observer outside the system. Several key concepts of duct acoustics will be reviewed.

2.2.1 Duct Cross-Sectional Eigenfunctions

The wave equation in the frequency domain is known as the Helmholtz equation,

$$\nabla^2 \tilde{p} + k^2 \tilde{p} = 0, \quad (2.4)$$

where the wave number $k = \omega/c$. A derivation is provided by Pierce[27] for the eigenfunctions of a rigid duct of any cross section. A separable solution of the Helmholtz equation in dimensions x , y , and z of the form

$$\tilde{p}(x, y, z) = X(x)\Psi(y, z), \quad (2.5)$$

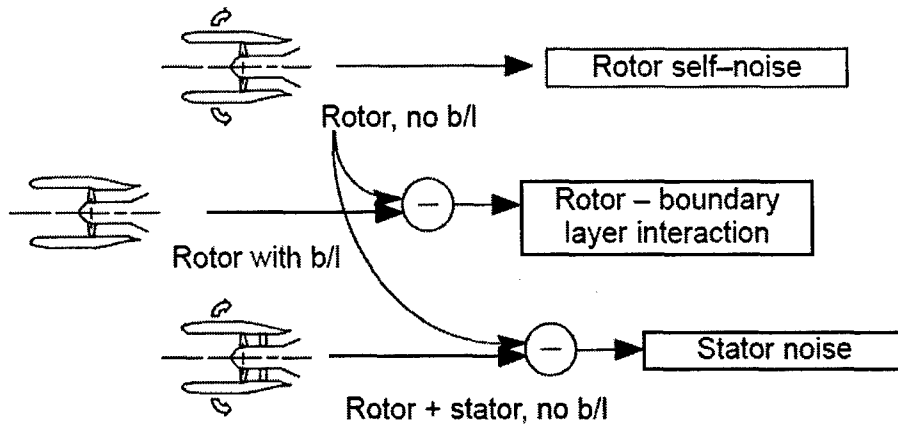


Figure 2.3. Experimental sound source separation method used in Ganz et al.[26].

where the duct is aligned with the dimension x . Separation of variables leads, for separation constant α^2 , to the differential equations

$$\left(\frac{\partial^2}{\partial y^2} + \frac{\partial^2}{\partial z^2} \right) \Psi + \alpha^2 \Psi = 0 \quad (2.6)$$

$$\frac{d^2 X}{dx^2} + (k^2 - \alpha^2) X = 0. \quad (2.7)$$

The cross section of the duct is governed by eigenfunction Ψ and eigenvalues α^2 . For a circular duct of radius a , the natural coordinate system is polar coordinates, with $y = r \cos(\phi)$ and $z = r \sin(\phi)$. Equation 2.6 is further separable, with solution $R(r)\Psi(\phi)$, where Ψ can be either $\cos(p\phi)$ or $\sin(p\phi)$, and where p is an integer. The radial function $R(r)$ satisfies the differential equation

$$\left[\frac{d^2}{dr^2} + \frac{1}{r} \frac{d}{dr} + \left(\alpha^2 - \frac{p^2}{r^2} \right) \right] R(r) = 0. \quad (2.8)$$

This is Bessel's equation, and has solutions $J_p(\alpha r)$ for a circular duct. The boundary condition for a rigid surface requires that $dR/dr = 0$ at the duct wall $r = a$, so the solution is only valid when $\alpha J'_p(\alpha a) = 0$. The values $\eta_{p,q}$ are used to denote the q th root of $\eta_{p,q} J'_p(\eta_{p,q}) = 0$. These values have been tabulated, and a few are noted in Table 2.1. The combined eigenfunction for the duct cross section is thus

$$\Psi(r, \phi) = K_{q,p} J_p \left(\frac{\eta_{p,q} r}{a} \right) \left\{ \begin{array}{l} \cos(p\phi) \\ \sin(p\phi) \end{array} \right\} \quad (2.9)$$

Plane waves are the 0,0 mode, and are always able to propagate in a duct. Higher order modes only propagate for frequencies $f > \eta_{p,q} c / 2\pi a$, in which case they are said to be *cut-on*. For the duct used in this experiment with radius of 0.103 m, the first mode is cut-on above 977 Hz. The mode shapes for a few higher order modes are shown in Figure 2.5.

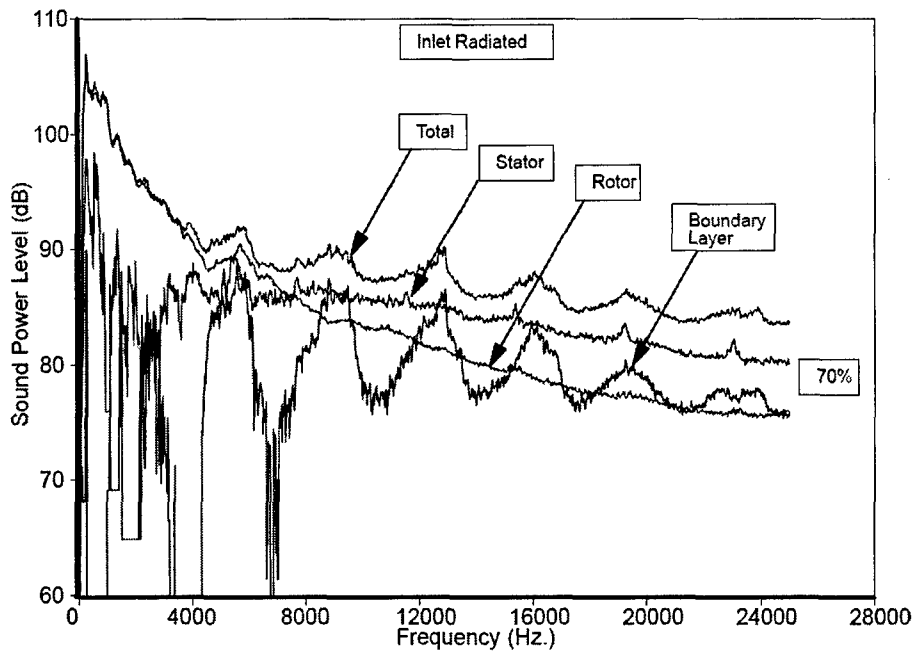


Figure 2.4. Results of sound source separation experiment from Ganz et al.[26].

2.2.2 Duct Organ Pipe Modes.

Reflection of acoustic waves can cause constructive and destructive interference, leading to amplification and attenuation of certain frequencies. When a plane wave travelling in a duct reaches an open end there is a change in acoustic impedance and a fraction of the energy is reflected back into the duct, while the remainder propagates out of the duct. An impedance change occurs at the duct termination and the duct to appears longer than its physical dimensions. The part of the wave that is reflected back can set up standing waves in the duct, which are known as organ pipe modes. The corrected length of a circular duct was calculated by Levine and Schwinger[28] to have an end correction of 0.6133 times the radius of the duct at low frequencies. For a duct with two open ends the fundamental organ pipe mode is therefore given as,

$$f_0 = \frac{c}{2(L + 0.6133(2R_d))}. \quad (2.10)$$

2.2.3 Analytical Free Space Dipole Green's Function

The far field sound from a point dipole can be predicted analytically by the free space Green's function. A development of the far field sound from point dipole sources is available in both Pierce[27] and Blake[2] and is summarized in the following. In this section the derivation considers only a point forcing in an unbounded fluid at rest.

	$q = 0$	$q = 1$	$q = 2$
$p = 0$	0.0	3.832	7.016
$p = 1$	1.841	5.331	8.536
$p = 2$	3.054	6.706	9.969

Table 2.1. Roots (η) of the first derivative of the first kind of Bessel function

$$\eta_{p,q} J'_p(\eta_{p,q}) = 0.$$

The Green's function G_m is defined as the solution to the inhomogeneous Helmholtz equation,

$$\nabla^2 G_m(\mathbf{r}, \mathbf{r}_0, f) + k^2 G_m(\mathbf{r}, \mathbf{r}_0, f) = -\delta(\mathbf{r}_0) \quad (2.11)$$

where the right hand side is a point monopole source at location \mathbf{r}_0 and the observer is at location \mathbf{r} . For a point source in an unbounded medium, an expanding spherical wave gives rise to the free space Green's function,

$$G_m = e^{ikr}/4\pi r, \quad (2.12)$$

where $r = |\mathbf{r} - \mathbf{r}_0|$.

A dipole is a superposition of monopole sources a small distance d apart (locations $\mathbf{r}_0 + \mathbf{d}/2$ and $\mathbf{r}_0 - \mathbf{d}/2$) and π out of phase. If $kd \ll 1$ this system is known as a point dipole. The combined transfer function is therefore $G_m(\mathbf{r}, \mathbf{r}_0 \pm \mathbf{d}/2)$. As long as $r \gg d$, the combined transfer function can be approximated with a truncated Taylor series as

$$G_m(\mathbf{r}, \mathbf{r}_0 \pm \mathbf{d}/2) \approx G_m(\mathbf{r}, \mathbf{r}_0) \pm (\mathbf{d}/2) \cdot \nabla_0 G_m(\mathbf{r}, \mathbf{r}_0), \quad (2.13)$$

where ∇_0 indicates the gradient with respect to the source coordinates. The pressure field from this point source is

$$\tilde{p} = \mathbf{D} \cdot \nabla_0 G_m(\mathbf{r}, \mathbf{r}_0), \quad (2.14)$$

where \mathbf{D} is the *dipole-moment amplitude vector*. The dot product can be reduced to

$$\tilde{p} = |\mathbf{D}| |\nabla_0 G_m(\mathbf{r}, \mathbf{r}_0)| \cos \phi = |\mathbf{D}| \frac{e^{ikr}}{4\pi r^2} (ikr - 1) \cos \phi, \quad (2.15)$$

where ϕ is the angle between the axis of the dipole and the observer. The term

$$|\nabla_0 G_m(\mathbf{r}, \mathbf{r}_0)| = \frac{e^{ikr}}{4\pi r^2} (ikr - 1) \cos \phi \quad (2.16)$$

can be called the free space dipole Green's function, and this result was used in the data processing method that is discussed in Section 4.

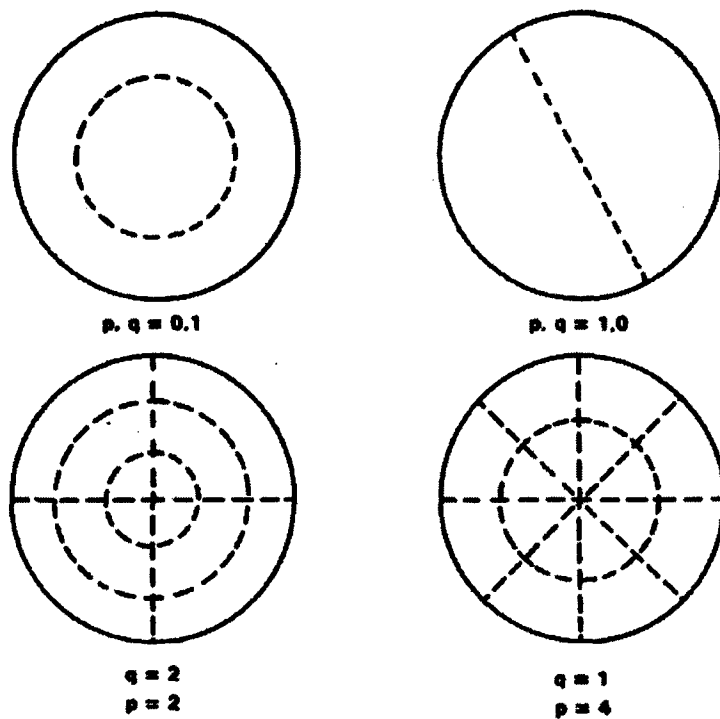


Figure 2.5. Illustrations of mode shapes for circular duct acoustic modes; q = number of node circles, p = number of node diameters. Figure from Blake[2].

SECTION 3

Experimental Setup

An experimental model of a ducted rotor was constructed in an anechoic chamber, as illustrated in Figure 3.1. The model was designed such that the fluid dynamic and acoustic boundary conditions could be manipulated and quantified. The duct was constructed from PVC with a machined inner diameter of 0.206 m and a wall thickness of 0.013 m, and supported by a vibration isolation pad. A center cylinder extended upstream of the duct inlet and downstream of the outlet to create an annular flow passage. The inlet flow was conditioned using a thin fabric with negligible acoustic impedance stretched over a cylindrical wire frame. A compact servo motor was housed in the center cylinder to direct drive the rotor at the desired speed. The upstream cylinder and motor were supported by eight streamlined struts. The downstream center cylinder was cantilevered from a support structure beyond the duct outlet (not shown).

The rotor was a ten-bladed propeller used by Sevik[29], with diameter $R = 0.101$ m, constant blade chord $C = 0.025$ m and maximum thickness of 2.4 mm, and straight blades incorporating twist only. The rotor operated with a tip gap equal to 5% of the blade chord. The length of the duct was variable, as was the location of the rotor within the duct.

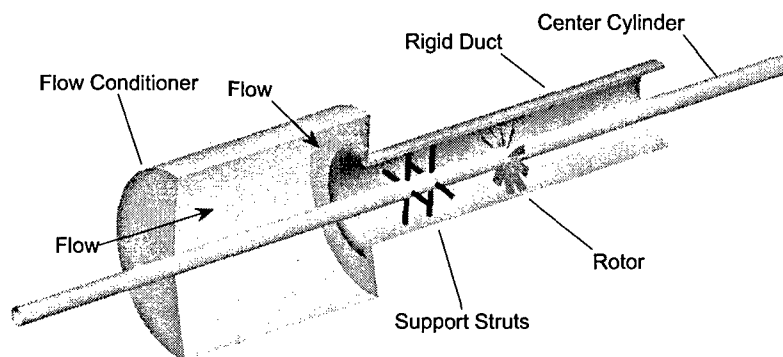


Figure 3.1. Schematic of experimental model.

3.1 Flow Field Measurements

A single straight wire probe was used to acquire time resolved measurements in the approach flow to the rotor and in the rotor wake. The probe was traversed in the radial and azimuthal directions downstream of the support struts and 5 cm upstream of the rotor. Measurements in the wake of the rotor were also conducted with a straight wire, oriented such that it would be most sensitive to velocity in the \vec{r} and \vec{x} directions. The probe was located 7 mm downstream of the rotor and traversed radially from the outer diameter of the duct to the inner hub. The probe was located at an azimuthal location between two of the support struts. A shaft phase signal was acquired from the motor controller so that phase mean and phase RMS velocity could be computed.

3.2 Microphone Measurements

Radiated sound was measured using Brüel & Kjær capacitance based microphones sampled at 40 kHz. Two single far field microphones were used, at distances of 1.8 and 1.3 meters from the duct inlet and angles of 9.5 and 45 degrees from the axis of the duct, respectively. For all of the results presented in this document, the 1.8 meter microphone was used. Note that this position provided a direct line of sight to part of the rotor. Initial measurements utilized a beamforming array. However, this was found to provide little benefit compared to single microphone results due to the low background noise of the AWT facility. Microphone measurements were acquired at all rotor speeds at the operating conditions noted on Fig. 3.2. The data were processed into spectral densities with frequency intervals of 4.8 Hz. The anechoic facility limited the useful range of measurement to only frequencies above 100 Hz.

3.3 Experimental Parameters

The following list describes the experimental parameters that were varied as part of the completed work.

Rotor Speed The servo motor system was capable of driving the rotor at a specified speed between 0 and 5000 RPM. For most of the data acquired to date, 11 rotor speeds were used between 2500 and 5000 RPM. This is important for the data processing method described in Section 4.

Duct Length The rigid plastic duct was constructed in short sections such that it would be easy to add and remove pieces to change the total duct length. Overall length can currently be varied between 0.62 and 1.4 meters.

Approach Turbulence The inlet flow was conditioned using a porous cloth at the entrance to the duct. The character of the turbulence was controlled by placement of the support struts and by modifying the casing boundary layer characteristics.

Operating Condition The back pressure in the duct was increased by adding flow resistance in the form of thin cloth, and decreased by attaching the outlet of the duct

to the fan system of the wind tunnel. A characteristic curve for the rotor was documented, as shown in Fig. 3.2, where the non-dimensional flow rate in the duct is given by $\phi = U_0/V_{tip}$ and the non-dimensional pressure rise across the rotor is given by $\psi = \Delta p / \frac{1}{2} \rho V_{tip}^2$. The detailed acoustic and flow field measurements were acquired at four operating points: $\phi = 0.42$ representing zero pressure rise, $\phi = 0.30$ as a typical design operating point, $\phi = 0.22$ as the maximum pressure rise, and $\phi = 0.17$ where the rotor was in rotating stall.

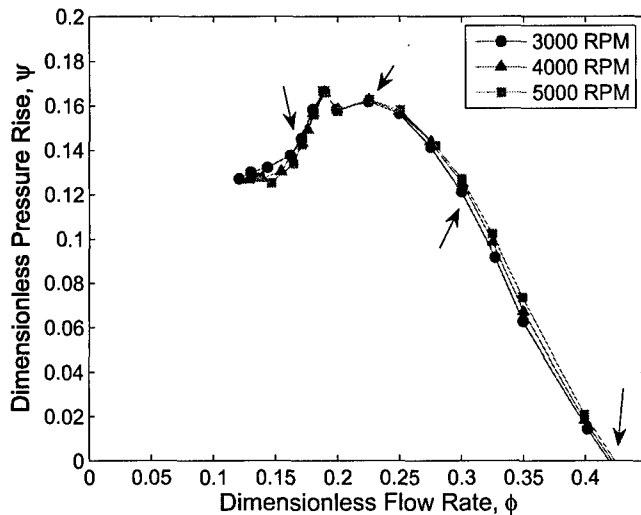


Figure 3.2. Dimensionless rotor characteristic curve. Arrows denote operating conditions where detailed measurements were made.

SECTION 4

Blocked Model Calculation of Transfer Function

Acoustic measurements acquired from the ducted rotor experiment were found to exhibit spectral features that were significantly dependent on the geometry of the duct system. The duct acts to amplify or attenuate specific frequencies such that the radiated sound spectra is modified from the sound source spectra. In order to study the sound sources in this system using far field microphone measurements a method was needed to account for the duct transfer function effects. A similar decomposition of measured sound was previously considered by Mongeau et al.[30]. This section describes a new method for decomposing radiated sound spectra into features due to the sound source and features that are part of the acoustic transfer function between the source and the microphone location.

4.1 Blocked Modeling Representation

The propagation of sound waves in low Mach number aeroacoustic problems is governed by the inhomogeneous Helmholtz equation

$$\nabla^2 \tilde{p}(\mathbf{r}, f) + k^2 \tilde{p}(\mathbf{r}, f) = -\tilde{\sigma}(\mathbf{r}_0, f), \quad (4.1)$$

where \tilde{p} is the Fourier transform of the unsteady acoustic pressure. The term $\tilde{\sigma}$ is the Fourier transform of the acoustic source $\sigma = \partial^2 T_{ij} / \partial x_i \partial x_j$, where T_{ij} is the Lighthill stress tensor. The Green's function $G(\mathbf{r}, \mathbf{r}_0, f)$ for this equation is defined the same way as in Section 2.2.3, however the boundary conditions are different due to the specific rigid geometry of the duct system. The solution to Equation 4.1 for rigid walled systems is an integral over all the distributed sources at locations \mathbf{r}_0 , and the Green's function between those points \mathbf{r}_0 and the observer location \mathbf{r} , such that

$$\tilde{p}(\mathbf{r}, f) = \iiint_V \tilde{\sigma}(\mathbf{r}_0, f) G(\mathbf{r}, \mathbf{r}_0, f) dV(\mathbf{r}_0). \quad (4.2)$$

Following the derivation of Blake[2], if the distance $r = |\mathbf{r} - \mathbf{r}_0|$ between source and receiver is larger than the wavelength under consideration and if $r \gg |\mathbf{r}_0|$ such that the observer is far outside the source region, then the receiver is in the acoustic far-field and the Green's function can be separated. The effects due to time retardation between source and receiver, the true spatial distribution of sound sources and Doppler effects due to rotation of the

sources can be all be regarded as near-field effects, and the total Green's function can be expressed as

$$G(\mathbf{r}, \mathbf{r}_0, f) = G_{far}(\mathbf{r}, f) G_{near}(\mathbf{r}_0, f). \quad (4.3)$$

The sound propagation from immediately outside the source region to the receiver is accounted for in $G_{far}(\mathbf{r}, f)$ while near field acoustic effects within the source region are accounted for with $G_{near}(\mathbf{r}_0, f)$. Substituting Equation 4.3 into Equation 4.2, it is apparent that $G_{far}(\mathbf{r}, f)$ can be taken out of the integral over the source region, such that,

$$\tilde{p}(\mathbf{r}, f) = G_{far}(\mathbf{r}, f) \iiint_V \tilde{\sigma}(\mathbf{r}_0, f) G_{near}(\mathbf{r}_0, f) dV(\mathbf{r}_0). \quad (4.4)$$

For a finite measurement of length T , an estimate of the sound pressure autospectral density is defined as

$$\mathcal{P}(\mathbf{r}, f) = \frac{2}{T} E \{ \tilde{p}(\mathbf{r}, f) \tilde{p}^*(\mathbf{r}, f) \}, \quad (4.5)$$

where $E\{\cdot\}$ denotes the expected value, and the cross-spectral density of the source term is

$$\Phi_{\sigma\sigma}(\mathbf{r}_{01}, \mathbf{r}_{02}, \omega) = \frac{2}{T} E \{ \tilde{\sigma}(\mathbf{r}_{01}, f) \tilde{\sigma}^*(\mathbf{r}_{02}, f) \}. \quad (4.6)$$

An expression analogous to Equation 4.4 can be introduced in terms of these statistical quantities,

$$\mathcal{P}(\mathbf{r}, f) = |G_{far}(\mathbf{r}, f)|^2 \iiint_V \cdot \iiint_V \Phi_{\sigma\sigma}(\mathbf{r}_{01}, \mathbf{r}_{02}, \omega) G_{near}^*(\mathbf{r}_{01}, f) G_{near}(\mathbf{r}_{02}, f) dV(\mathbf{r}_{01}) dV(\mathbf{r}_{02}). \quad (4.7)$$

The right hand side of this expression can be written as a combination of two terms,

$$\mathcal{P}(\mathbf{r}, f) = \mathcal{D}(f) \mathcal{G}(\mathbf{r}, f), \quad (4.8)$$

where the source spectra \mathcal{D} represents an effective lumped acoustic source and includes acoustic propagation effects due to $G_{near}(\mathbf{r}_0, f)$ that may exist within the source region. The propagation of acoustic energy from the source to the far field is now represented as a single transfer function, $\mathcal{G}(f)$. This derivation of Equation 4.8 is similar to that given in Blake[2] for rotors in an open field and by Mongeau et al.[30] for the case of ducted rotors. The terms \mathcal{D} and \mathcal{G} are often termed the blocked source function and blocked transfer function because they represent an approximate integral representation of the true source distribution and Green's function, respectively.

It is of interest to consider the frequency range for which the compact source assumption is valid. Blake[2] suggests that Equation 4.8 is valid so long as the sources are distributed over a spatial extent that is less than one quarter of the acoustic wavelength. This corresponds to frequencies of less than 855 Hz for the ducted rotor used in the present experiments based on the duct radius of 0.1 m. This roughly corresponds to the cut-on frequency of higher order modes of the duct. The data that are presented below, however, demonstrate that Equation 4.8 is a reasonable approximation at significantly higher frequencies.

4.2 Fundamental Frequencies of the Ducted Rotor System

The issue that is addressed in this section can be stated as follows. Given measurements of radiated pressure, can the source and transfer functions be independently determined? If only one set of measurements is available, it is obvious from Equation 4.8 that this is not a well posed problem. However, Mongeau et al.[30] suggested that multiple measurements of the radiated sound \mathcal{P} at different rotor speeds Ω will allow for the separation of specific features of the source and transfer function spectra. Consider, for example, that local maximum in the spectra that are related to blade rate tones will occur at a frequency that increases linearly with the rotational speed of the rotor. In contrast, spectral features related to the geometry of the system, such as organ pipe modes of the finite length duct, will occur at a fixed frequency, independent of the rotor speed.

The sound field generated by a ducted rotor can be considered to have two inherent frequencies. The first is related to the relative motion of the blades with respect to the approach flow. Following the notation proposed by Mongeau et al.[30], a Strouhal number can be defined using the blade tip velocity as

$$St = \frac{2\pi R_t f}{V_{tip} B}. \quad (4.9)$$

This scaling and notation is justified by the fact that the sound sources will depend on the fluid dynamics of the blade-flow interactions.

The second frequency scale is related to the geometry, and can be normalized by a length scale of the geometry and the speed of sound. Again following the notation used by Mongeau, the Helmholtz number is defined as

$$He = \frac{2R_d f}{c_0}. \quad (4.10)$$

The measured sound spectral density has dimensions of pressure² / frequency. For use in this algorithm we consider a sound spectra \mathcal{P} with dimensions of pressure², where the density has been integrated to account for the frequency bin width. The dipole Green's function as derived in Section 2 has dimensions of 1/Area, and so the dimensions of \mathcal{G} are 1/Area. The dimensions of the unsteady dipole source are force, and \mathcal{D} has dimensions of force². Expressing the functions of interest in terms of decibels, and using the notation $X = \log \mathcal{X}$, Equation 4.8 can be written as

$$P(f) = D(St) + G(He). \quad (4.11)$$

The objective of the present effort was to exploit the dependence of D on the rotational speed, Ω , in order to use the measured P to obtain estimates of both D and G . By inspection of Equation 4.11, there is clearly a limitation for any algorithm to separate D from G . For example, absolute magnitude of D and G can not be determined. Additionally, linear dependence ($D \propto St$, $G \propto He$) can not be separated by changing the rotor speed, and can not be distinguished. In contrast, consider a feature of the sound source spectra that is very narrow in shape. For this feature, a large change in the rotor speed will move the center frequency of the feature, and allow the determination of the feature separate from the fixed

transfer function spectra. In the results below, the size of large and small features and how well they can be resolved by the presented algorithm is quantified in terms of a dimensionless feature size and the ratio of the maximum to the minimum speed tested.

The two frequency scales are illustrated in Figures 4.1 and 4.2, which show measured sound spectra $P(\Omega, f)$ from the ducted rotor experiment in dB referenced to 20μ Pa. A number of distinctive features were observed in the spectra, including narrow band tones at multiples of the blade passing frequency, and broad local “humps” which remained at a fixed frequency location as the rotor speed was increased. Significant broad band sound was also observed at high frequency. The transfer function $G(He)$ has features that are aligned in f , and remain at fixed locations in f as source speed is increased, as seen in Figure 4.1. Normalizing frequency by blade passing frequency aligns the features of the sound spectrum that are dependent on the source terms, such as blade passing tones, as shown in Figure 4.2. These two frequency scales are utilized in the separation algorithm that is presented in Section 4.4.

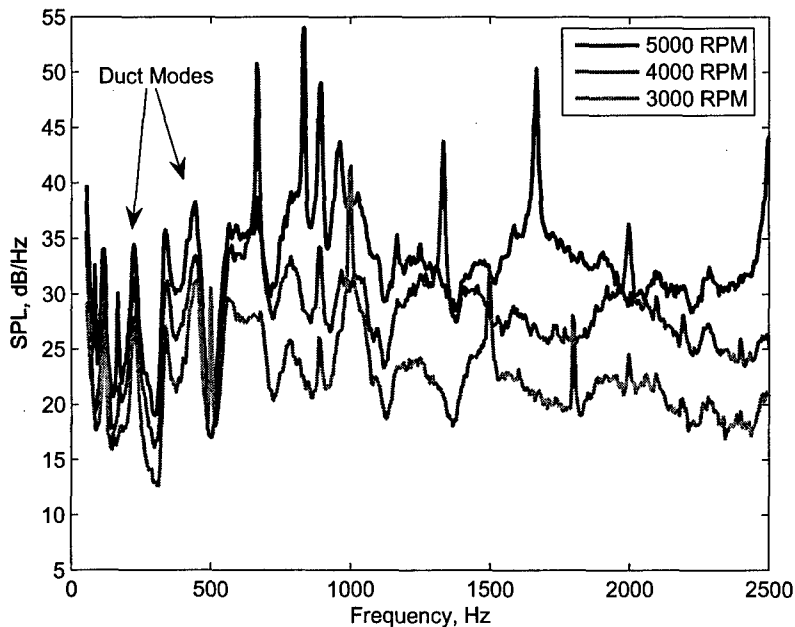


Figure 4.1. Measured sound spectra for ducted rotor at three rotational speeds.

4.3 Review of Previous Work

As already noted, the separation of blocked source spectra from an acoustic transfer function using microphone measurements was first considered by Mongeau et al.[30]. It is

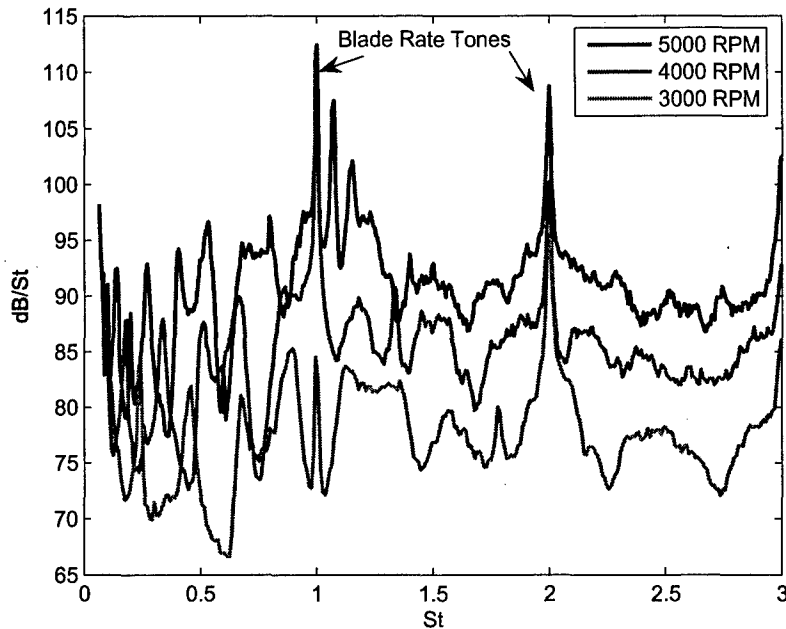


Figure 4.2. Measured sound spectra for ducted rotor at three rotational speeds, frequency normalized as St .

therefore appropriate to comment on their method, and note the differences between their work and the present effort. An attempt to use their method for the present measurements presented a number of challenges. First, the previous work assumed a fixed acoustic scaling that may not hold in general. Specifically, they assumed that the source spectra would increase as the cube of the rotational speed. Not only was that found not to be the case for the present experiments, but it was found that the scaling exponent (denoted n below) was found to be a strong function of the Strouhal number. Secondly, the method relies on using an integrated adjustment to the transfer function magnitude in order to create a continuous curve, and many features in this integrated region are lost. Finally, the user is required to specify an interval of St in the calculation. The results were found to be strongly dependent on the values chosen.

The method developed in this paper does not assume a value for the tip scaling, and the resulting transfer function is determined from all of the available data, rather than at short integration regions. Additionally, the efficacy of the present method was investigated using mathematically defined input functions, as described in Section 4.5.1.

4.4 Source-Transfer Function Separation Method

4.4.1 Aeroacoustic Scaling Model

An algorithm was developed that separates experimentally obtained sound spectra $P(\Omega, f)$ into source spectra $D(\Omega, St)$ and the transfer function spectrum $G(He)$. The method utilizes the two frequency scales inherent in the system and seeks to incorporate the least restrictive assumption about the functional form of the sound source spectra. The algorithm assumes that a function \mathcal{D}_0 exists, such that the source spectra at all rotor speeds is given by

$$\mathcal{D}(\Omega, St) = \mathcal{D}_0(St) U_{tip}^{n(St)}, \quad (4.12)$$

where the exponent n is explicitly a function of St and is solved for in the algorithm. This scaling relationship simplifies the problem by incorporating the dependence of the sound source on rotor speed into $U_{tip}^{n(St)}$. Taking the logarithm, Equation 4.12 can be rewritten as

$$D(\Omega, St) = D_0(St) + n(St) \cdot \log(U_{tip}). \quad (4.13)$$

In words, the logarithm of the source $D(\Omega, St)$ is expected to increase linearly with $\log(U_{tip})$. Deviations from this scaling were assumed to have been caused by transfer function effects.

The objective of the method can be summarized as follows. The algorithm seeks to find a function $G(He)$ that can be subtracted from the measured sound $P(\Omega, f)$ such that the source spectra $D(St)$ scales linearly with the log of rotor tip speed $\log(U_{tip})$. Such a function would account for the features of Figure 4.1 that remain at a fixed frequency as the rotor speed is increased.

4.4.2 Implementation as a Computer Algorithm

The algorithm was implemented in Matlab on a desktop computer. Processing time ranged from less than a minute to several minutes, depending primarily on the number of points in the frequency spectra.

Step 1: Estimate Source Spectra as $D_{guess}(\Omega, f) = P(\Omega, f) - G_{guess}(f)$. An initial guess of $G(He) = gg^*$ was made, as introduced in Section 2.2.3, and $D_{guess}(\Omega, f) = P(\Omega, f) - G_{guess}(f)$ was used to start the algorithm. The frequency axis of the estimated sound source spectra was then normalized by BPF to obtain $D_{guess}(\Omega, St)$, and the magnitude of D_{guess} was also scaled by $|BPF|$ to conserve the integrated sound pressure. Linear interpolation was used to obtain the spectral magnitudes at discrete values of St from $D(\Omega, f)$.

It was important to consider the scaling of the frequency axis and restrict the calculations to the extent of the available data. Specifically, the highest useable frequency was determined by the highest St of the highest speed. As an example, the maximum measured sound frequency of 20 kHz corresponded to $St = 48$ at 2500 RPM, and $St = 24$ at 5000 RPM, so the highest St that could be used was 24. The limit of the estimates for $D(St = 24)$ likewise correspond to frequencies of 10 kHz to 20 kHz, so the lower value of 10 kHz must be used in rescaling the functions back to frequency in Step 5 below. The useable range of frequencies was therefore reduced by $1/SR$, where the speed ratio $SR = \Omega_{max}/\Omega_{min}$. The lower limit of the useable range was determined by experimental uncertainty, such as the useable frequency range of the anechoic facility. A minimum useful frequency of 100 Hz for

the present measurements corresponded to $St = 0.24$ for 2500 RPM and $St = 0.12$ for 5000 RPM. The minimum usable value of $St = 0.24$ was used, which corresponded to 100 Hz at 2500 RPM and 200 Hz at 5000 RPM. The frequency range of usable data is reduced at both ends by the scaling.

Step 2: Find $n(St)$ using a linear fit to $D_{guess}(\Omega, St)$ vs $\log(U_{tip})$. According to the model given in Equation 4.13, at each value of St , a plot of $D(\Omega, St)$ vs $\log(U_{tip})$ should be a straight line with slope $n(St)$. An example from the ducted rotor experiment is shown in Figure 4.3 at $St = 1.1$. The presence of $G(He)$ in the data causes some points be moved off of the linear scaling, and these are considered outliers. For the ducted rotor experiment, $D(\Omega, St = 1)$ spans a frequency range from 416 to 833 Hz and measurements were obtained at 11 speeds between 2500 and 5000 RPM. When one or more of these samples is amplified or attenuated due to a duct mode or other effect they are moved off of the linear scaling. The unknown function $n(St)$ was determined using an ordinary least-squares fit, as well as a robust linear fit method, as described by Huber[31]. The robust fit was implemented using the `robustfit()` command in Matlab and is an iterative weighted adaptation of the least-squares method, which reduces the influence of outliers on the linear fit. The linear fit was made for all values of St in order to determine $n(St)$.

Step 3: Estimate $\overline{D}_0(St)$ using Equation 4.13 and $n(St)$. An estimate for $D_0(St)$ for each speed Ω was found using $n(St)$ determined in Step 2, $D_{guess}(\Omega, St)$ from Step 1 and Equation 4.13. The estimates from each Ω were averaged at each St to obtain $\overline{D}_0(St)$. The minimum and maximum values at each St were removed before averaging, in an additional effort to remove outliers.

Step 4: Obtain $D_{new}(\Omega, St)$ using $n(St)$ and $\overline{D}_0(St)$. From Equation 4.13 it is possible with $n(St)$ from Step 2 and $\overline{D}_0(St)$ from Step 3 to get an improved guess for $D(\Omega, St)$, denoted $D_{new}(\Omega, St)$.

Step 5: Obtain $G(He)$ using measured sound $P(\Omega, f)$ and $D_{new}(\Omega, St)$. The source spectra $D_{new}(\Omega, St)$ were rescaled to get $D(\Omega, f)$, and interpolation was again required to get data at the same points as the original power spectra in f . An estimate of $G(He)$ is obtained for each rotor speed using the measured sound spectra $P(\Omega, f)$, $D_{new}(\Omega, f)$ and Equation 4.11. These these estimates were averaged over all speeds to get $G(He)$.

Step 6: Use new estimate for $G(He)$ to iterate from Step 1. Between one and three iterations were found to provide a balance between a converged solution and a useful frequency range in the result. The example data from the ducted rotor at the same points from Figure 4.3 are shown in Figure 4.4 after one iteration. This indicates the transfer function features have been largely captured in $G(He)$, and the linear scaling is seen to be much improved.

4.5 Evaluation of Separation Method

4.5.1 Error Analysis of the Algorithm

A set of defined input functions was constructed in order to evaluate the effectiveness of the algorithm. The set consisted of a function for $G(He)$, a function for $D_0(St)$ and a scaling $n(St)$. A series of artificial power spectra $P(\Omega, f)$ were created using Equations 4.11 and 4.13 and used as input into the algorithm. The resulting function for $G(He)$ could then be

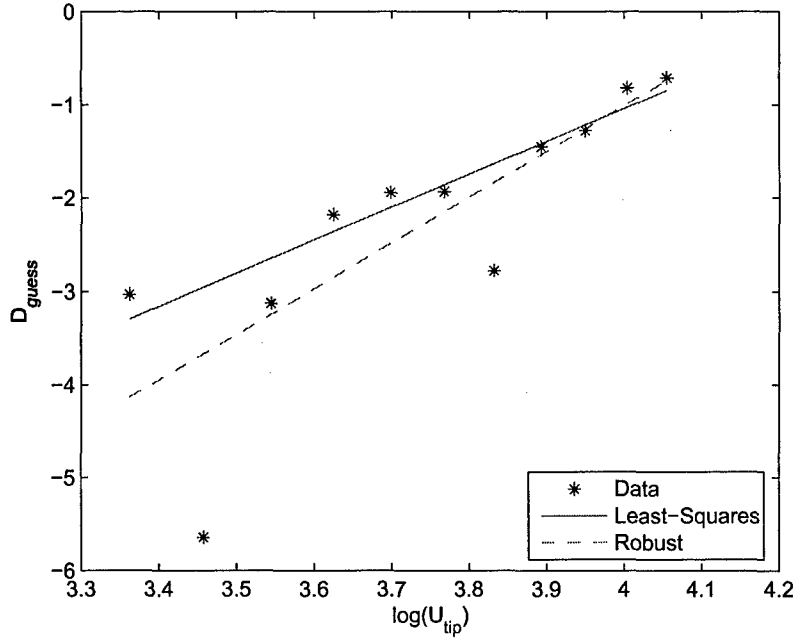


Figure 4.3. Experimental data showing linear fit to $D_{guess}(St)$.

compared to the input, and an error computed by comparing the calculated transfer function (G_C) to the actual transfer function (G_A) as

$$Error = \sqrt{\frac{\int [G_C(f) - G_A(f)]^2 df}{\int [G_A(f)]^2 df}}. \quad (4.14)$$

The transfer function G_A used for the defined input function set was a gaussian curve with a parameterized frequency width Δf and center frequency f_c given as,

$$G_A = e^{-10(f-f_c)^2/\Delta_f^2} \quad (4.15)$$

and shown in Figure 4.5. The feature shape can be considered a worst case, since the values were only positive and only induced outliers on one side of the correct linear slope in the $D(\Omega, St)$ vs $\log(U_{tip})$.

A series of transfer functions were tested over a range of f_c and Δ_f and the error was computed. It was found that the error could be described by the functional relationship

$$Error = function\left(\frac{\Delta_f}{f_c}, SR\right). \quad (4.16)$$

Specifically, the error curves at each SR collapsed when plotted against the *feature size ratio*, Δ_f/f_c . This is reasonable because the range of f spanned at fixed St is a linear function

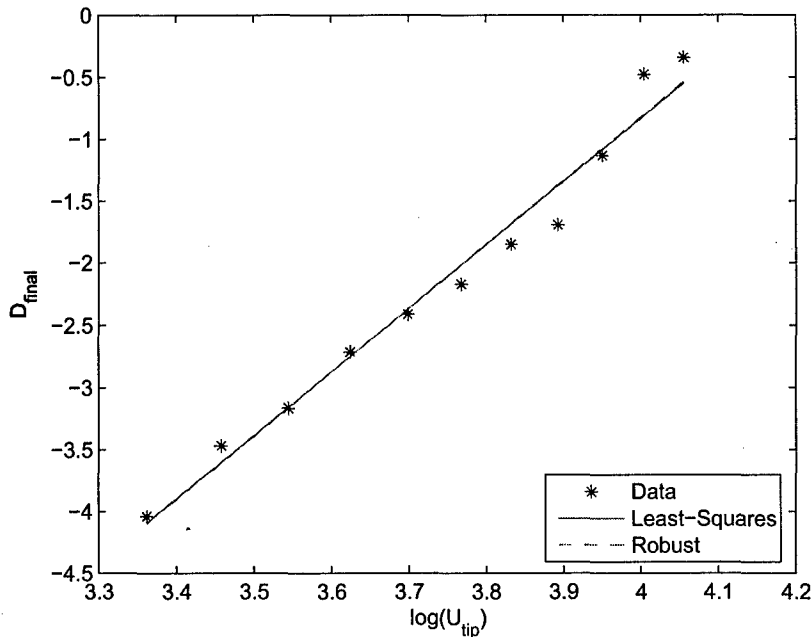


Figure 4.4. Experimental data showing sound source linear scaling after transfer function has been removed.

of St . In this experiment, at $St = 1$ the 11 speeds span 416 to 833 Hz while at $St = 10$ the range is between 4160 and 8330 Hz. Lower St values result in frequency ranges that are small, such that if the transfer function changes only slightly across the frequency range it will not be well resolved. The apparent size of a feature therefore depends on its center frequency 'location,' f_c , as well as its frequency 'width,' Δ_f .

The successful identification of transfer function features is also dependent on the speed ratio used during measurement. A small speed ratio results in points that are close together in f at constant St and only transfer function features that cause changes in that range of frequency will be identified. A larger speed ratio allows larger features to be identified. Minimum and maximum rotor speeds represent a physical limit to the experimental data that can be obtained. Conversely, larger speed ratios effect the frequency range of the output when computing the scaling between $St \Leftrightarrow He$, as discussed in Steps 1 & 5.

The error functions defined by Equation 4.16 are shown in Figure 4.6. For one specific set of defined input function tests using $SR = 2$, a feature of size 0.1 was 99.6% resolved in one iteration and 99.92% resolved after two iterations, while a feature size of 0.2 was 95% resolved in one iteration and 97% resolved after three iterations. Small features are well resolved under all speed ratios while larger features are poorly resolved. A higher speed ratio leads to lower error, especially for larger feature size ratios.

The only assumption made regarding the nature of the source spectra was the scaling

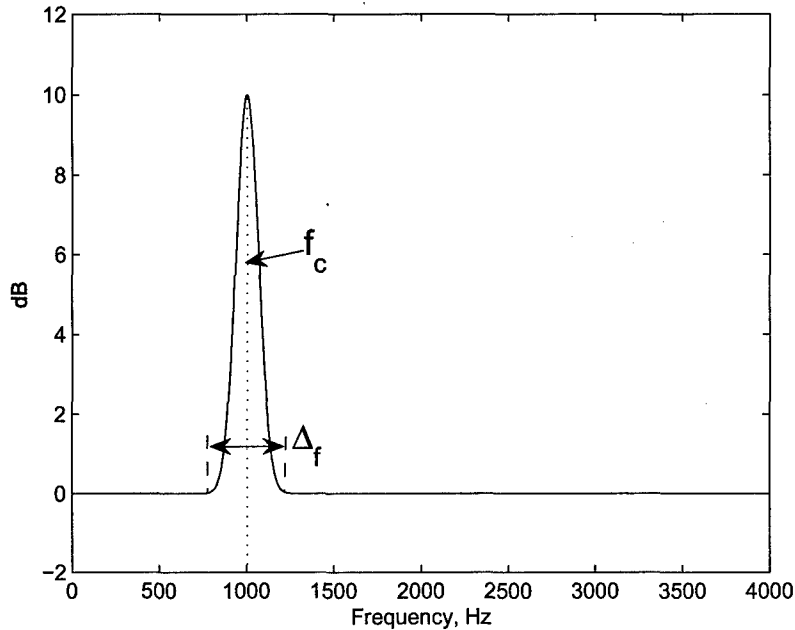


Figure 4.5. Example simulated transfer function.

relationship given by Equation 4.13. It was therefore of interest to simulate how well the algorithm resolved features in $G(He)$ when the source did not follow this type of scaling. For example, acoustic compactness is directly related to the ratio of the acoustic wavelength to the blade size. If this were the dominant effect, $n(f)$ would be a more appropriate scaling law than $n(St)$. It was found that the ability of the algorithm to obtain the correct function $G(He)$ was unchanged by these differences in the functional form of n .

As a final note on the algorithm, a minimum of three points was required to use a least-squares linear fit. Good convergence of the $G(He)$ curves at different loading conditions was found when five or more speeds were used.

4.5.2 Separation Algorithm Applied to Varied Sound Source Data

Another test of the algorithm was to use data acquired using the same geometry with a variety of rotor sound sources. This would change the sound source under constant transfer function conditions. The sound source was found to be significantly dependent on the rotor blade loading,

$$\psi = \frac{\delta p}{1/2\rho U_{tip}^2}, \quad (4.17)$$

such that $D(\Omega, \psi, St)$. The blade loading was increased by applying various restrictions to the duct exit that had negligible effect on the acoustic field, and decreased by attaching the

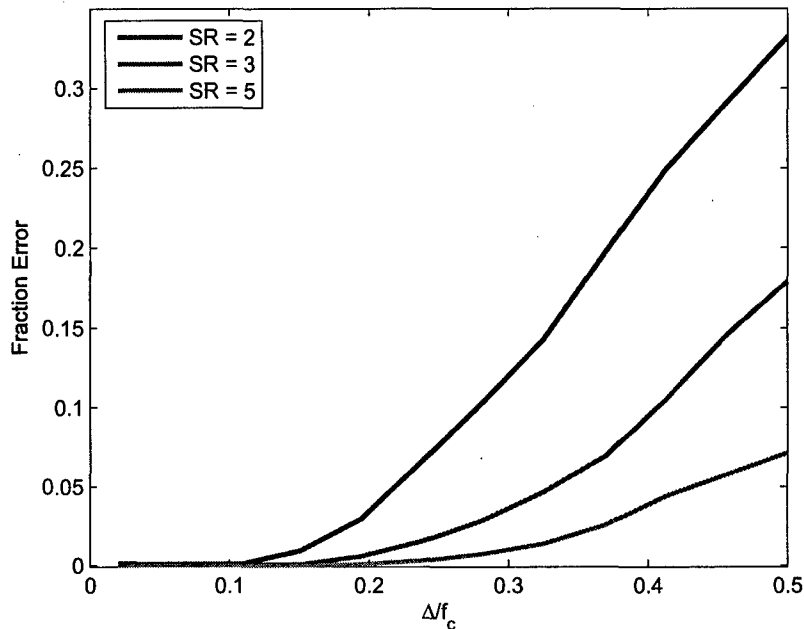


Figure 4.6. Error for different values of *feature size ratio* and speed ratio after three iterations.

outlet of the duct to the anechoic wind tunnel blower. The radiated sound from four loading cases was measured at 11 speeds from 2500 to 5000 RPM. The spectra for $\Omega = 5000$ RPM are shown in Figure 4.7. Substantial changes in the sound produced by the system were observed, indicating that the source spectra was a strong function of ψ .

The transfer function from the various blade loading cases are shown in Figure 4.8 for two iterations of the algorithm, using the far field dipole transfer function as an initial guess. While the measured sound spectra were quite different, the geometry of the experiment remained the same in all cases so there should be no change to the transfer function. This was found to be the case, as the four transfer functions returned by the algorithm were all very similar. The standard deviation between the four curves at each frequency was taken, and a mean value of 0.26 dB was found.

The frequency axis shown in Figure 4.8 was normalized by the first organ pipe frequency based on duct length L calculated as in Equation 2.10. The harmonics of predicted organ pipe modes are seen to correlate with peaks in the resultant transfer function.

The algorithm also calculated the best fit slopes for $n(St)$. Note that scaling the frequency axis to St effectively increases n by 1 from the equivalent value for $n(f)$. The results for the four loading cases are shown in Figure 5.7, where a small amount of smoothing has been applied to reduce small scatter due to interpolation error and the statistical convergence of the spectral calculation. The scaling with tip speed was found to be a complicated function of $n(St)$, with peaks at integer multiples of blade passing frequency, and reduced

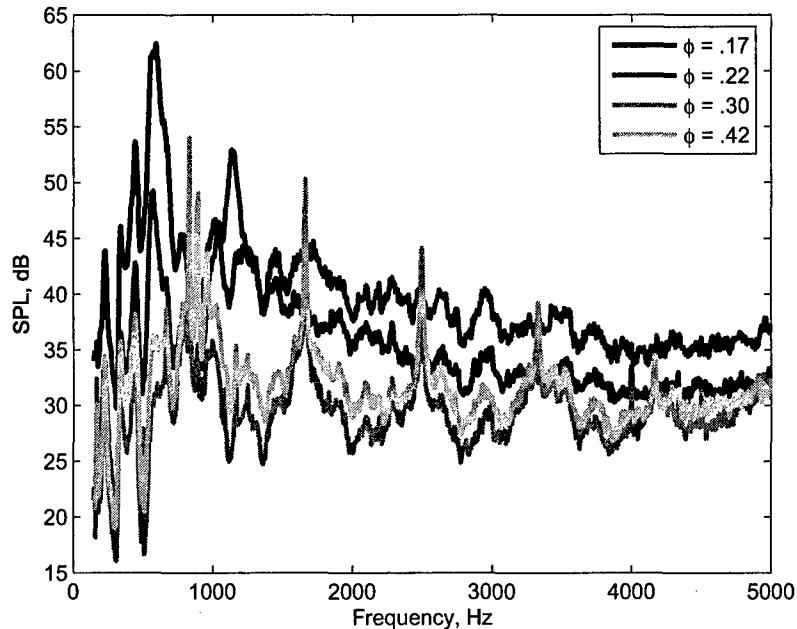


Figure 4.7. Measured sound under different loading conditions at 5000 RPM.

sound power output scaling with higher values of St . Values of $5 < n < 6$ are expected for dipole sound.[2]

4.5.3 Separation Algorithm Applied to Varied Transfer Function Data

The separation algorithm was evaluated by operating the experimental system with various duct lengths. This allowed the transfer function to be changed while keeping the sound source constant. By keeping the distance between the rotor and the inlet fixed the approach turbulence was kept constant. The downstream duct length was changed with only minimal effect on the sound sources. A possible change to the sound source could come from increased loading on the rotor blades due to pipe friction from the longer duct lengths, but the pressure rise across the rotor under these different conditions was found to be nearly the constant. The differences to the transfer function are not as great in this case as the differences in the sound sources under different loading conditions, so this test is not as rigorous as the previous case. Figure 4.9 shows the radiated sound with different duct lengths. Note that the transfer function as shown in Figure 4.8 has diminishing feature magnitudes at higher frequencies, so even with different duct lengths the radiated sound agrees to within about 2 dB above 3500 Hz. Figure 4.10 shows transfer functions from two different duct lengths, illustrating magnitude differences of more than 10 dB. The algorithm was used to identify the sound source spectra, and the results are shown in Figure 4.11. The resulting

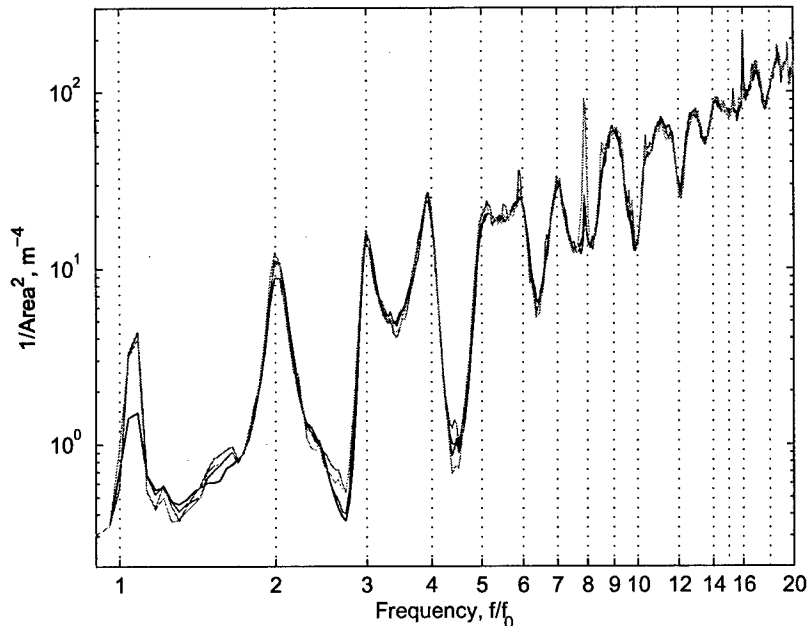


Figure 4.8. Calculated transfer functions for $\phi = 0.17, 0.22, 0.30$ and 0.42 between 216 and 4791 Hz, normalized by the first organ pipe mode. Note that the first organ pipe mode ($f/f_0 = 1$) is at 112 Hz, which is at the lower limit of the usable frequency range of the anechoic facility.

sound sources are seen to be within 2.5 dB above about 1000 Hz, while lower frequencies do show some discrepancies. This are possibly due to the difficulty in capturing features with large size ratio ($\Delta f/f_c$), as defined in Section 4.5.1. The resulting agreement between the sound source spectra again support the validity of the blocked model. As expected, the different duct lengths result in different transfer functions, but similar sound sources.

4.6 Summary of Separation Algorithm

A technique for processing aeroacoustic measurements was developed and evaluated. The method utilized the two frequency scales that are inherent in many aeroacoustic systems to determine the functional form of a blocked source and a blocked acoustic transfer function given radiated sound spectra at various flow speeds. This technique was implemented as a computer algorithm, and evaluated with mathematically defined input functions, as well as experimental results from a low speed ducted rotor. The following conclusions can be taken from these measurements:

- Any separation of blocked sources and blocked transfer function will require some form

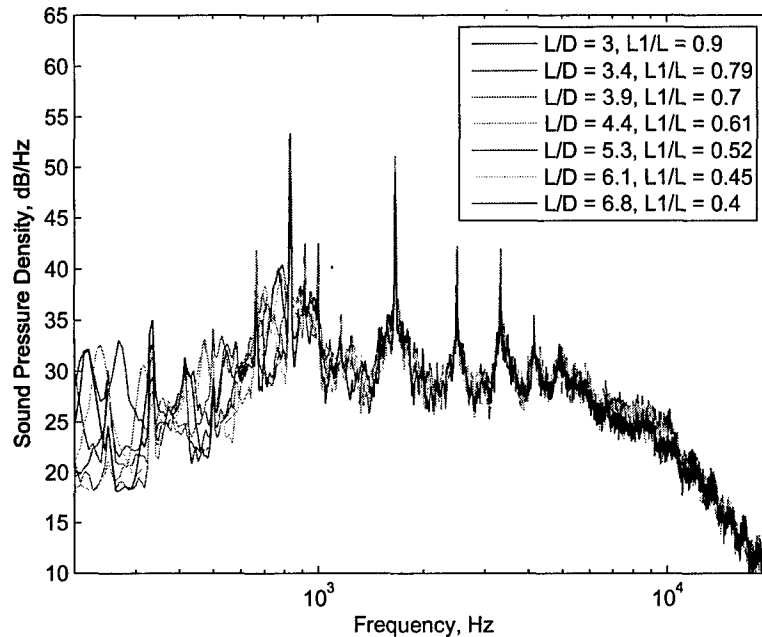


Figure 4.9. Measured sound at 5000 RPM for varying duct lengths.

of assumption about either the source or the transfer function spectra. In the present algorithm, the acoustic source was assumed to increase with rotor speed to an unknown power.

- The ability of the algorithm to determine spectral features was determined. Specifically, features whose width to center frequency ratio $\frac{\Delta f}{f_c} < 0.1$ were found to be 99% resolved for a speed ratio of 2.
- The initial guess for the transfer function was selected to be the free space dipole transfer function. Thus the absolute magnitude and large scale trend of the transfer function were prescribed by this form. Features small enough to be identified were found to be superimposed on the free space dipole transfer function.
- The algorithm was applied to process experimental data and a transfer function was recovered for a ducted rotor model. Transfer functions were calculated for varied source conditions and were found to closely agree, with a standard deviation of 0.26 dB. The method effectively removes transfer function features from measured sound in a system where a blocked dipole source term is an appropriate approximation.
- The spectral character of the ducted rotor transfer function was found to have peaks of magnitude up to ± 10 dB at integer multiples of the first duct organ pipe mode, in addition to other complicated features.

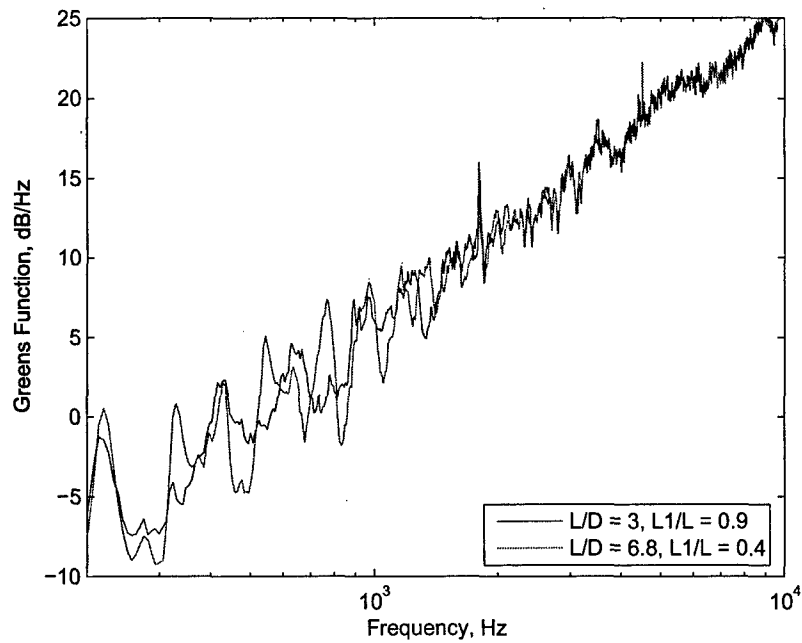


Figure 4.10. Transfer function result for different length ducts.

As a final comment, the algorithm developed should be equally applicable for any aeroacoustic system with two frequency scales, not only for ducted rotor systems. The method has also been applied to study high speed turbomachinery.

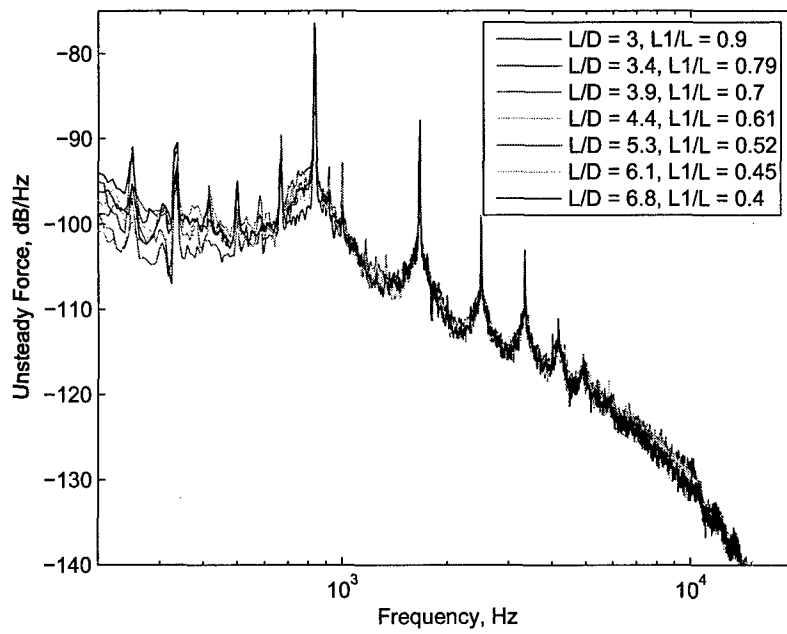


Figure 4.11. Sound source spectra at 5000 RPM for varying duct lengths.

SECTION 5

Flow Field and Acoustic Source Results

Sound generation in low Mach number turbomachines is typically dominated by unsteady fluid forces on rigid surfaces. As a result, the radiated sound is closely related to the unsteady flow field. Measurements of the flow field around a ducted rotor are used in the present investigation in order to provide insight to the various mechanisms of sound that are present at different mean loading conditions. Despite the identified importance of mean blade loading on sound, there is still relatively little experimental data available that describes the acoustics of ducted rotors at "off-design" conditions. Such information is not only valuable for applications where the operating point is allowed to vary, but can also serve to separate various sources within the rotor. As an example, sound generated by tip leakage flow can be eliminated by setting the operating point such that there is no net lift at the blade tips.

5.1 Flow Fields Results

One of the primary motivations of the present study was to provide a direct link between the acoustics generated by the rotor and the surrounding flow field. This section will present velocity statistics upstream and downstream of the rotor in order to document the basic characteristics of the flow at the four loading conditions identified in Figure 3.2. A description of the acoustic signatures in terms of the flow field observations will be provided Section 5.2.

The time mean and RMS contours of the approach flow are shown in Figure 5.1. The dominant features were the wakes of the support struts which caused velocity deficits, reducing axial velocity to about 0.9 times the spatially averaged velocity in the duct U_0 . The RMS axial velocity in the free stream was less than $0.01 U_0$, while in the wake of the support struts the RMS velocity was increased to about $0.05 U_0$. Turbulent boundary layers can be observed at the hub and tip radii, where the peak RMS levels were found to be $0.09 U_0$. Velocity spectra were measured and typical results are shown in Figure 5.2. The flow in the boundary layer is seen to have the most spectral energy, while the undisturbed flow between the support struts has very low turbulence levels, and the sharp peaks are actually acoustic motions due to tonal noise generated by the rotor.

The phase mean measurements from the rotor wake survey are shown in Figure 5.3 for the four different loading conditions. Phase RMS measurements are shown in Figure 5.4. For reference the mean angle of attack experienced by the blades at several radial locations was calculated and are given in Table 5.1. Note that all of the measurements were obtained at a rotor speed of 3750 RPM. The characteristic curves shown in Figure 3.2 suggest that

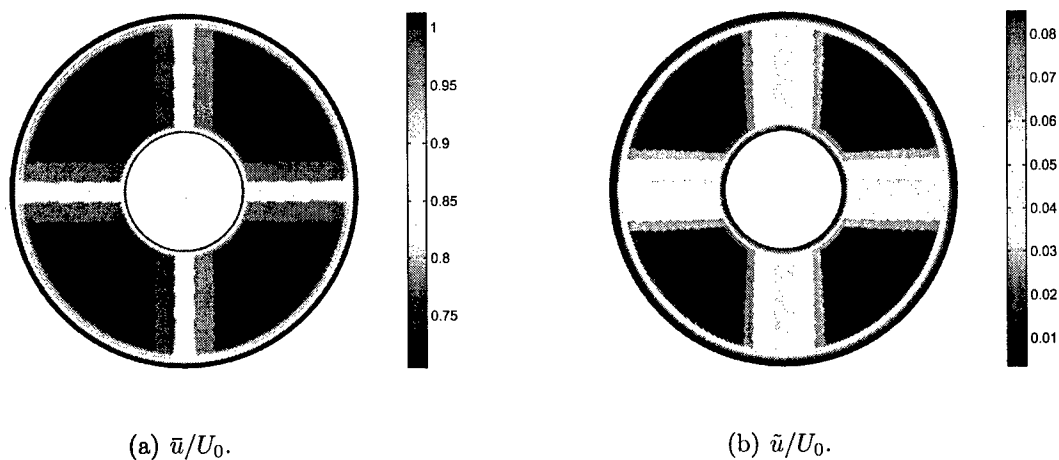


Figure 5.1. Mean and RMS of axial component of velocity in plane $x/R_{tip} = 0.25$ upstream of rotor.

the flow is essentially independent of Reynolds number, and the dimensionless data can be considered to be representative for the speed range used in the acoustic measurements. The following summarizes the observations observed at the four mean loading conditions.

$\phi = 0.42$ This operating point was selected to represent a case in which the blades were at nearly zero angle of attack, and thus did not raise the static pressure in the duct. The phase mean data shown in Figure 5.3 at this loading condition indicate that the axial distribution of velocity is nearly uniform, and equal to the nominal value of 0.42 as set by the operating point. Narrow wakes from the 10 blades can be observed in the mean velocity, and are distinct in the RMS values shown in Figure 5.4. The relatively large magnitude of the unsteadiness in the wakes ($\tilde{u}/U_0 \approx 0.07$) could have resulted from turbulent boundary layers on the blades, or unsteadiness in the blade wake as observed from the rotating reference frame.

$\phi = 0.30$ This operating condition was chosen as a probable design condition with moderate loading, but at a flow rate that is safely higher than the stall point. The relative flow angles are less than 10 degrees over the entire span, and the blade boundary layers appear fully attached. The RMS contours show lower unsteadiness in the blade wakes over most of the span than was found at the higher flow rate. In addition, a small but well defined tip structure is evident in the wakes, as indicated by small regions of large RMS levels. This suggests that fluid flow at the blade tips is attached, but highly three dimensional in nature due to the tip leakage flow.

$\phi = 0.22$ This operating condition represents the highest pressure rise on the rotor characteristic. The mean angle of attack is moderate near the tip, and relatively high (>16 degrees) near the hub. The mean velocity in the tip regions was reduced, although the magnitudes were higher than one might expect for fully separated flow. Note also

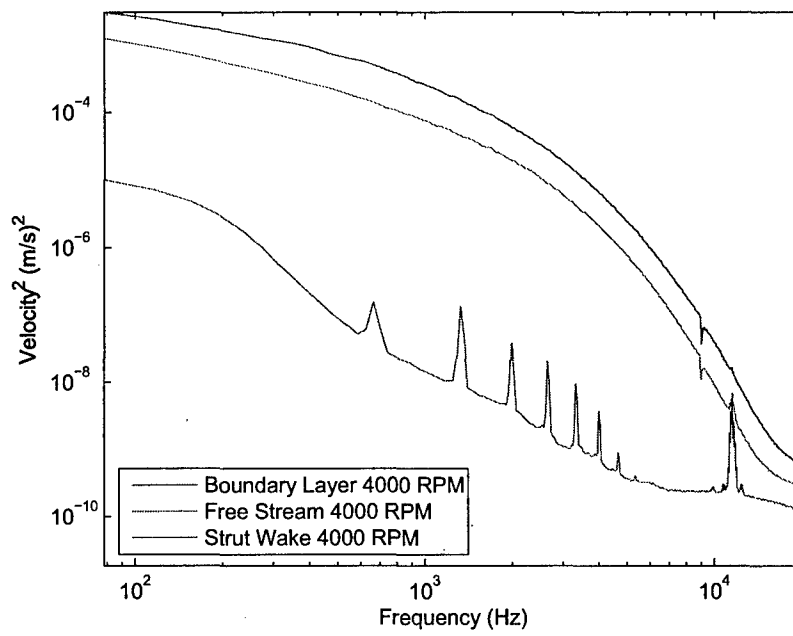


Figure 5.2. Velocity spectra of approach flow in plane $x/R_{tip} = 0.25$ upstream of rotor.

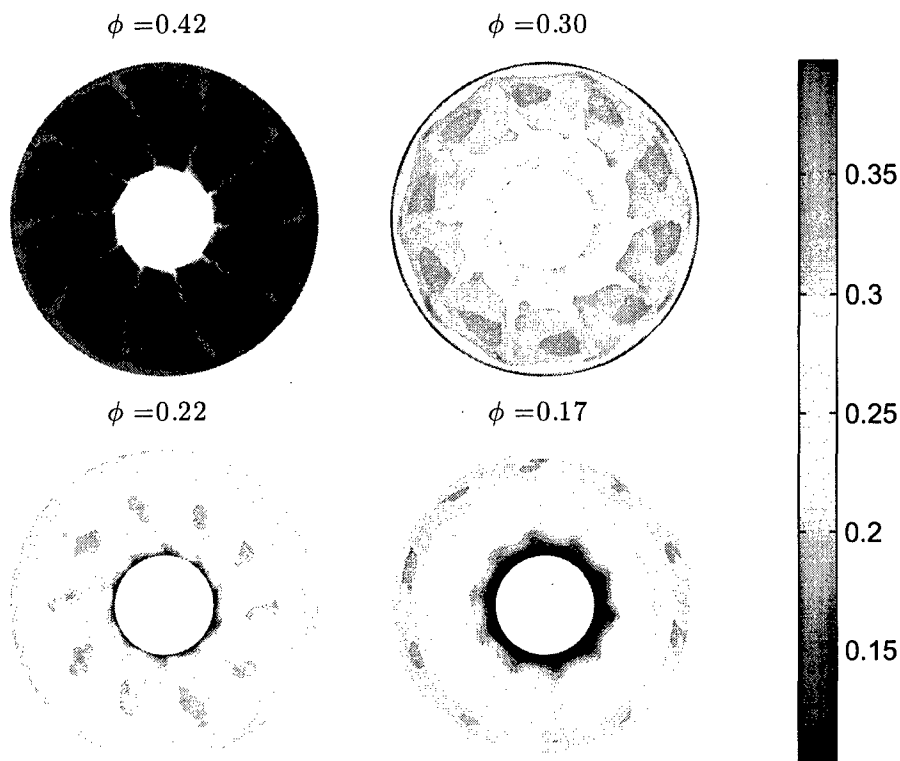


Figure 5.3. Phase mean velocity \bar{u}/U_0 measured at $x/R_{tip} = 0.031$.

the the RMS contours show a well defined large scale tip flow structure with increased unsteadiness levels.

$\phi = 0.17$ At this condition blades are past the stall angle over most of the span, and pressure rise is lower than that obtainable at the higher flow rate. Although the blades are likely in some type of rotating stall, a significant axial velocity can still be observed over the entire span. A well defined blade wake structure can be observed in the RMS contours near the hub, as the flow is likely attached to the blades. The tip structure is significantly less organized compared with the previous condition.

Figure 5.5 shows velocity spectra from the hot wire measurements near the tip of the rotor for the four different loading conditions. These data provide some additional information about the rotor flow field that will be useful in describing the acoustic results in the next section. Specifically, the $\phi = 0.42$ case has the lowest broadband unsteady velocity levels while levels at all the other flow rates are similar. At the highest two flow rates significant peaks at blade rate harmonics are observed, while the lower flow rates feature little or no unsteady component at these frequencies. Note the broad humps at lower frequency are likely related to a part span stall condition. Specifically, multiple stall cells rotating at a fraction of the rotor speed could result in the spectra shown. This possibility will be discussed in

	$\phi = 0.42$	$\phi = 0.30$	$\phi = 0.22$	$\phi = 0.17$
$r = R_{hub} = .25R_{tip}$	-1.2	7.9	16.7	23.9
$r = .50R_{tip}$	-0.1	9.0	16.2	21.2
$r = .75R_{tip}$	-0.7	6.7	12.2	15.8
$r = R_{tip}$	-1.6	4.5	8.8	11.6

Table 5.1. Mean angle of attack α in degrees for rotor blade under different loading conditions.

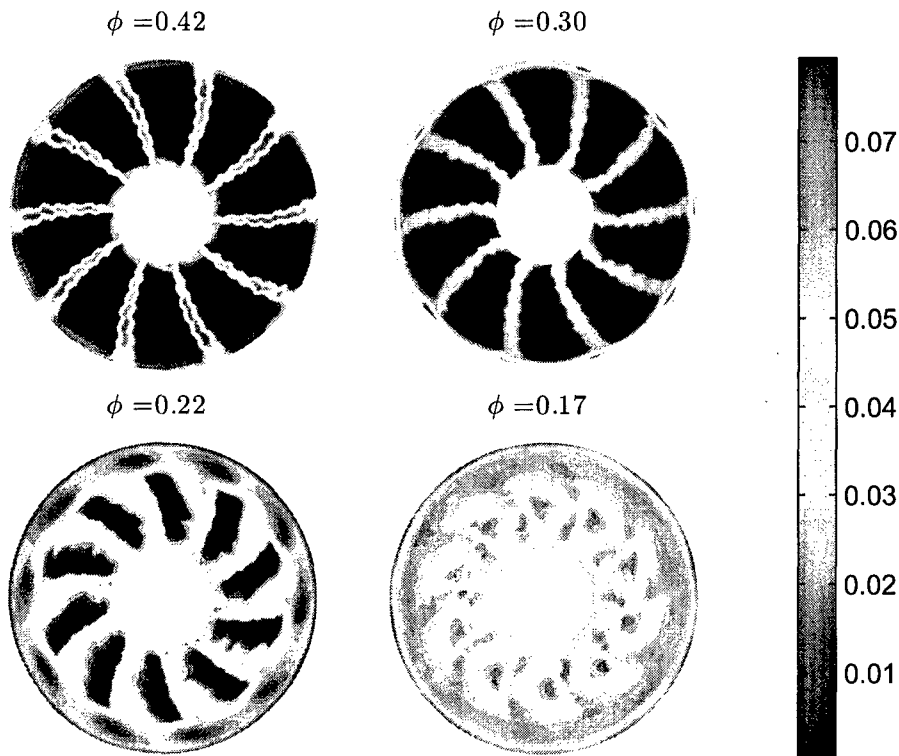


Figure 5.4. Phase RMS velocity \bar{u}/U_0 measured at $x/R_{tip} = 0.031$.

more detail in the following section.

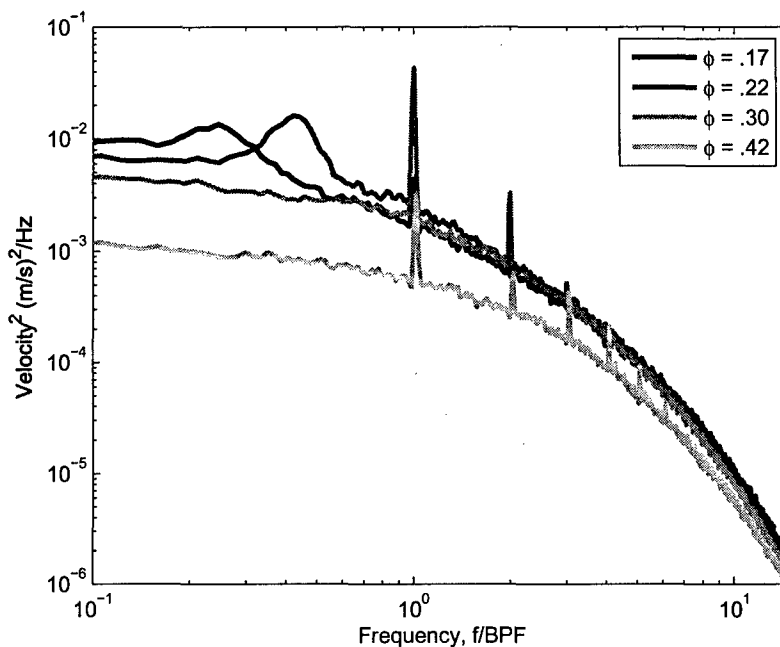


Figure 5.5. Autospectral density of axial velocity at $r/R_{tip} = 0.98$, $x/R_{tip} = 0.0625$.

5.2 Sound Source Variation with Operating Point

5.2.1 Unsteady Force Spectra

The sound generated by a low speed axial rotor can be considered as a superposition of independent source mechanisms, each of which can be classified as either interaction noise or self noise. Interaction noise in the present geometry can result from the interaction of the blades with the mean velocity deficit and turbulence caused by the upstream support struts, as well as the turbulent boundary layers at the hub and duct walls. Self noise can result from a number of phenomena, including the interaction of the blade boundary layers with the trailing edge, unsteady wake flows, three dimensional tip flow, flow separation and lift breakdown, and rotating disturbances.

The radiated sound measurements were acquired at 11 speeds for each of the four loading conditions described in Section 3.3. The spectral values were post-processed as described in Section 3.2 in order to provide the sound source spectra as an unsteady lift. These results are presented in decibels, with a reference force of dynamic pressure based on tip speed times rotor cross sectional area, $F_{ref} = \frac{1}{2}\rho V_{tip}^2 \pi R_{tip}^2$. These results are shown in Figure 5.6 for the 5000 RPM measurements. The following points of interest have been observed in the data.

$\phi = 0.42$ The source spectra for the two highest flow rates were found to be similar, and both were dominated by tonal sound at integer multiples of the blade passing frequency. The length scale of the strut wakes are large and periodic so that multiple blades interact with the disturbances in phase, resulting in fluctuating forces that are correlated between blades. Small scale turbulence in the approach flow is a source of broadband sound, and the slow roll-off with frequency of the source spectra suggest that there is a wide range of turbulent length scales. Note that one previous study[26] has experimentally investigated the broad 'pedestals' around the blade rate tones and found them to disappear when the duct outer boundary layer was removed by suction.

$\phi = 0.30$ The moderate loading case produced the lowest level of radiated sound. The decrease in the mean axial velocity from the $\phi=0.42$ condition corresponds to a 28% decrease in the magnitude of the turbulent fluctuations in the approach flow, and a 4% reduction in the blade relative velocity. Given the unsteady lift from these interactions should scale with $\tilde{u}^2 U_0^2$, a 3.4 dB reduction in the unsteady lift would be expected. This is consistent with the observed reduction in sound of approximately 3 dB at $St < 4$. The phase RMS levels shown in Figure 5.4 show \tilde{u}/U_0 in the rotor wakes decreasing from 0.7 at $\phi = 0.42$, to 0.3 at $\phi = 0.30$. For frequencies $f/BPF > 6$ the source spectra results for $\phi = 0.30$ and $\phi = 0.42$ are nearly identical. This suggests that the high phase RMS value for $\phi = 0.42$ shown in Figure 5.4 is a result of unsteady motions of the blade wakes, rather than turbulence in the blade boundary layers.

$\phi = 0.22$ A sub-blade rate peak and a second multiple were the dominant features of the source spectra. The first blade rate tone was still observed, although it is hidden in the figure. Higher order tones blade rate were found to be diminished to levels below that of the broadband, which was the loudest of any of the cases measured. The sub-blade rate peak was found to be centered around 0.68 BPF, with a louder second multiple and a much quieter third harmonic. These peaks are probably related to a stall phenomena that is rotating at less than the shaft rate. One possibility is that there are one or more part-span flow separations that exist in the blade row, and the tonal sound is related to the unsteady forces caused by the repeated stalling and recovery of lift.

$\phi = 0.17$ The blade rate tones were not observed in this case, even though the broadband level was below the tonal level peaks observed in the two highest flow rate cases. It is plausible that the largely separated flow led to the reduced tonal noise, as the turbulent structures in the approach flow do not remain attached to the rotor blades. This sound spectrum was also dominated by the tone at 0.68 BPF, with no higher multiples apparent. Future research using a circumferential array of hot-wires will provide a better understanding of these mechanisms of sound production. Another possible explanation for the large peaks at 0.6 BPF can be given in terms of the low frequency flow oscillation observed by Bragg et al.[32], where flow over an airfoil was found to separate and re-attach at a regular frequency. Bragg et al. found that this frequency occurred at a non-dimensional frequency $f_0 = fC \sin(\alpha)/U$ between about 0.017 and 0.028, which corresponds to half of the frequency of the peak at 0.68 BPF. This flow oscillation was found to be a full-span effect that occurs for airfoils which can experience a separation bubble starting at the leading edge[33].

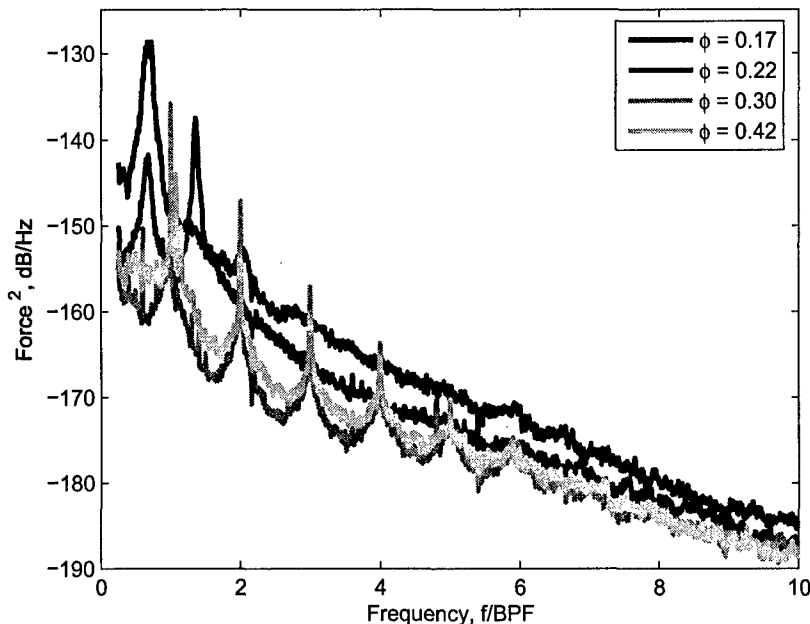


Figure 5.6. Sound source spectra for rotor at 5000 RPM.

5.2.2 Sound Source Scaling

It is of interest to consider how the aero-acoustic sources scale in magnitude with velocity. Specifically, $\mathcal{P} \propto U_{tip}^n$ is assumed in the decomposition algorithm introduced above, and the scaling $n(St)$ is determined simultaneously with the transfer function. Note that scaling the frequency axis to St effectively increases $n(St)$ by 1 from the equivalent value for $n(f)$. Different scaling spectra were found for each of the four different loading conditions, and are shown in Figure 5.7. At the highest flow rate ($\phi = 0.42$), the blade rate tones were observed to scale at $n \approx 1$ higher than the broadband sound. The broadband for all loading cases was highest in the range $St = 4 \rightarrow 8$, dropping off at higher frequencies. The moderate loading case ($\phi = 0.30$) indicated the lowest overall power scaling of the conditions evaluated. The two lower flow rates were found to have similar broadband scaling, but with large values at the frequencies noted earlier in reference to rotating stall conditions, that is $n > 6$ for $St \approx 0.68$. Table 5.2 provides the mean scaling averaged over frequency, $\overline{n(f)} = \overline{n(St)} - 1$. The total sound pressure in dB is also given for the 5000 rpm case for reference.

5.3 Sound Source Results with Downstream Support Struts

The original design of the experiment placed the necessary support struts upstream of the rotor for two reasons, 1) to provide quantifiable turbulent inflow to the rotor and 2)

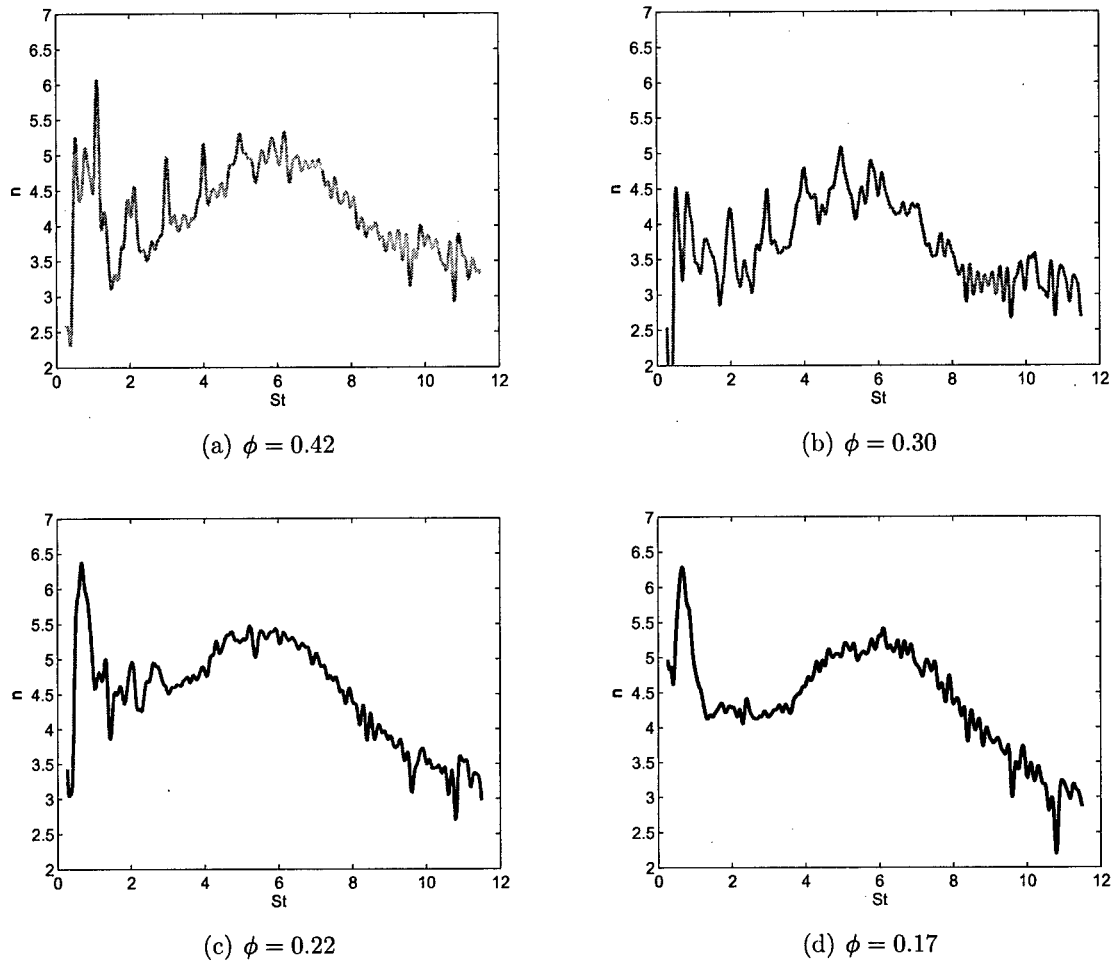


Figure 5.7. Power law scaling of rotor sound source.

	$\phi = 0.42$	$\phi = 0.30$	$\phi = 0.22$	$\phi = 0.17$
$n(f)$	3.22	2.71	3.51	3.37
SPL, dB	72.4	69.9	77.8	82.1

Table 5.2. Mean power scaling under different loading conditions and total decibel levels at 5000 RPM referenced to P_{ref} .

to eliminate the complicated wake flow interaction with downstream struts as a source of noise. All results described to this point are from operating the experiment with the struts upstream, as shown in Figure 3.1. A set of experiments was conducted with the support struts placed ($3.5R_d$) downstream of the rotor. The primary difference was expected to be in the approach noise, since the strut wakes in the approach flow as shown in Figure 5.1 would be absent. A typical result is shown in Figure 5.8. The expected result was that the broadband noise at low frequencies ($0 < f/BPF < 2$) went down, as would be expected from the reduced approach turbulence. The tonal sound was found to increase, as shown by the markers indicating the tones for the upstream strut case. This increased tonal noise may be due to the rotor wake impinging on the downstream struts but more measurements are needed to support this or other possibilities.

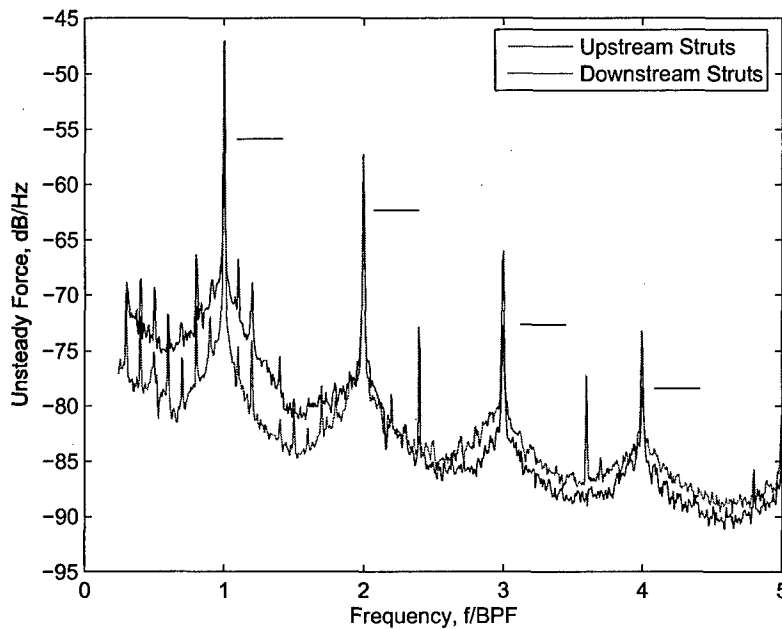


Figure 5.8. Sound source spectra for rotor at 5000 RPM comparing struts upstream and downstream configurations. Tonal peaks for upstream strut case marked with —.

5.4 Sound Source Variation with Tip Gap

With the struts in the downstream configuration, the rotor was studied with a larger tip gap. A section of duct with a smooth increase in diameter from the design dimension of 8.1 inches to a larger diameter of 8.15 inches was placed over the rotor blades, changing the tip gap from 5% to 7.5%. Both tip gaps were run at two operating points. The first was at $\phi \approx 0.30$. In this case, with sound source results shown in Figure 5.9, a decrease of 2 dB

between 0.4 BPF and 1 BPF. At a lower flow rate, $\phi \approx 0.20$, and decrease of 5 dB between 0.5 BPF and 0.8 BPF was observed, as shown in Figure 5.10. The larger tip gap seems to significantly reduce the broad peak due to rotating instability that was previously described at 0.68 BPF.

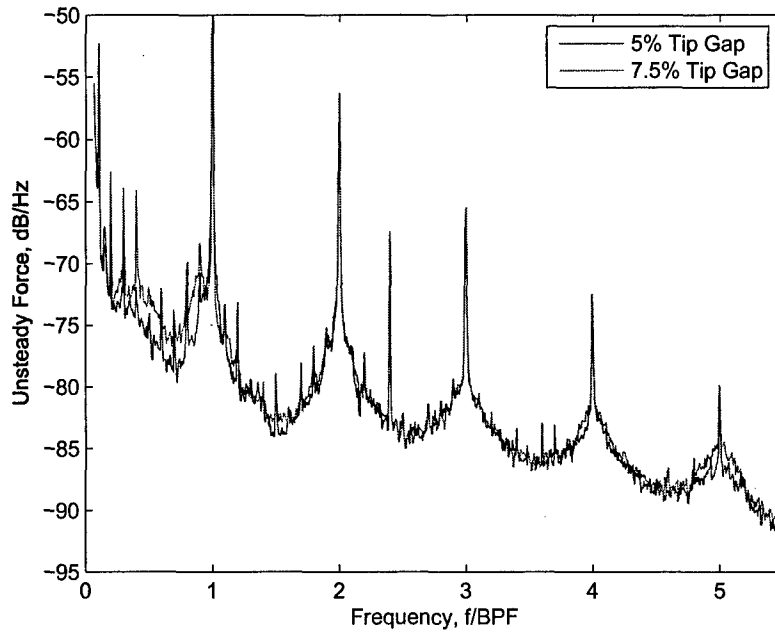


Figure 5.9. Sound source spectra for rotor at 5000 RPM with varied tip gap. $\phi = 0.30$.

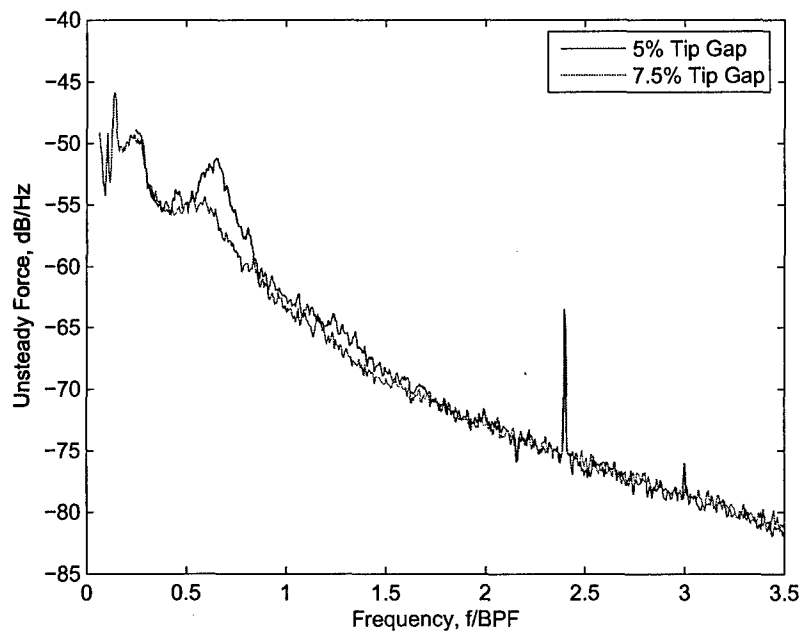


Figure 5.10. Sound source spectra for rotor at 5000 RPM with varied tip gap. $\phi = 0.20$.

SECTION 6

Conclusions

This report described the development and utilization of a new technique for studying radiated sound from aerodynamic sources operating inside rigid geometries. The rigid geometry of a duct system acts to amplify and attenuate particular frequencies of the sound source. A blocked modeling approach was used to identify transfer function effects from a series of radiated sound spectra. The rotor sound source was studied under a range of operating conditions and a number of sound producing mechanisms were identified. Flow field measurements were used to provide insight to the unsteady fluid motions that cause aerodynamic sound at subsonic flow speeds.

The separation algorithm provides a way to quantify amplifications and attenuations that are qualitatively apparent in radiated sound spectra and uses a series of measurements made at different rotor speeds to return a net transfer function. The blocked modeling equation was found to have fundamental limitations on the size of features that can be identified, independent of the algorithm, and these limitations were quantified through the use of a mathematically defined data set. The algorithm was also tested on experimental data, by changing the sound source only and verifying that the returned transfer function was constant. Additionally, the transfer function was changed independently of the sound source and the algorithm identified different transfer function spectra while the source spectra were found to agree to within about 3 dB over a wide frequency range.

A study of the effect of blade loading on the sound generated by a ducted rotor has been described. Radiated sound measurements were used to estimate the unsteady force spectra and these were related to unsteady flow field measurements upstream and downstream of the rotor. A number of conclusions were drawn from the calculated sound source spectra:

- Manipulating rotor loading provides provides a means to identify the separate sound sources. Different sound source mechanisms were found to dominate under different loading conditions. High and moderate flow rates were found to primarily produce interaction noise while at low flow rates the sound source spectra were dominated by broadband noise and low frequency broad peaks. Detailed fluid flow measurements provided insight into the different interaction and self noise mechanisms.
- Rotor noise is highly dependent on the operating point. Interaction noise identified by large blade rate tones and broad pedestals was dominant at high and moderate flow rates and increased scaling of blade rate tones was observed. At low flow rates the noise was primarily broadband, with little to no measurable sound at blade rate multiples.

- Flow separation over rotor blades has significant effect on generated sound. At the low flow rates interaction noise was found to be almost negligible. This is possibly due to flow separation over the rotor blades, which causes the approach turbulence to convect through the rotor but away from the rotor blades. At the same time, the stall phenomena leads to separation and recovery on the blades which is a source of unsteady forcing. The number and magnitude of stall cells is dependent on the operating point in the stall regime, but the frequency of the radiated sound was found to be at 0.68 BPF or higher harmonics.
- A minimum noise level operating point exists between the minimum and maximum pressure rise conditions. As shown in Table 5.2, the minimum radiated noise level and minimum sound power scaling were found at a moderate flow rate condition.

APPENDIX A

Evaluation of Blocked Modeling

As part of the development of the separation algorithm described in Section 4, a formulation was considered as a linear algebra problem. The combination of source and transfer function is expressed in log space as,

$$P_{rad} = \mathcal{D}(\Omega, \psi, \mathbf{u}(r, \theta), f) \mathcal{G}(L, L_1, \mathbf{r}, f). \quad (\text{A.1})$$

In logarithm space, as in decibels, this expression becomes a sum, with the notation $X = \log \mathcal{X}$,

$$P = D + G. \quad (\text{A.2})$$

Under the blocked modeling assumption, the terms D and G can be manipulated independently. For example changing the rotor speed changes the sound source, but not the transfer function, while moving to a different microphone location will change the transfer function G without changing the sound source D . This can be extended to consider several different radiated sound measurements, with different sound sources and different transfer functions, and this can be written as a linear algebra problem. As an example, for a fixed geometry, measurements made with different rotor speeds $n = 1 : N$,

$$\begin{aligned} P_1 &= D_1 + G \\ P_2 &= D_2 + G \\ &\cdot \\ &\cdot \\ P_n &= D_n + G. \end{aligned}$$

Considering different combinations of sources and transfer functions provides additional equations. Consider two speeds and two transfer functions:

$$\begin{aligned} P_{1,1} &= D_1 + G_1, \\ P_{1,2} &= D_1 + G_2, \\ P_{2,1} &= D_2 + G_1, \\ P_{2,2} &= D_2 + G_2, \end{aligned} \quad (\text{A.3})$$

which can be expressed in matrix form as $Ax = b$,

$$\begin{bmatrix} 1 & 0 & 1 & 0 \\ 1 & 0 & 0 & 1 \\ 0 & 1 & 1 & 0 \\ 0 & 1 & 0 & 1 \end{bmatrix} \begin{bmatrix} D_1 \\ D_2 \\ G_1 \\ G_2 \end{bmatrix} = \begin{bmatrix} P_{1,1} \\ P_{1,2} \\ P_{2,1} \\ P_{2,2} \end{bmatrix}. \quad (\text{A.4})$$

We find that that $\text{rank}(A) = 3$. This says that the system is underdetermined. There are not enough independent equations to find a unique answer. The fact that the equations are dependent means that any equation is a linear combination of the other three. For example, it means that $P_{1,1} - P_{2,1} - P_{1,2} + P_{2,2} = 0$. The minimum and maximum speeds at different loading conditions were selected to provide the biggest differences between sound sources $D_1(\phi = 0.42, \Omega = 2500 \text{ RPM})$ and $D_2(\phi = 0.17, \Omega = 5000 \text{ RPM})$. Two transfer functions were provided by two microphone locations with $r = 2\text{m}$ from the inlet and angles of 9.5 and 45 degrees. The sum is shown in Figure A.1. For reference, the four curves $P_{n,m}$ are shown in Figure A.2. The error is seen be within $\pm 3\text{dB}$ over most frequencies, with a few very narrow peaks of around 10 dB.

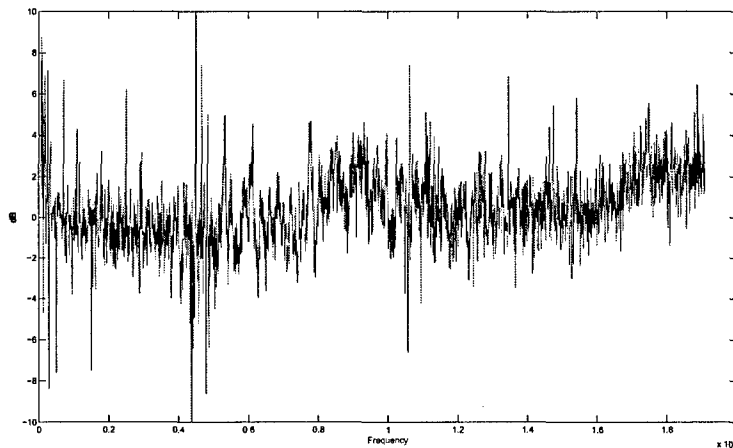


Figure A.1. Plot of $P_{1,1} - P_{2,1} - P_{1,2} + P_{2,2}$.

This method may provide a way to quantify the error in the blocked modeling assumption. If so then it is certainly worth pursuing a more rigorous analysis of the blocked model system. It may be that a blocked modeling assumption is not as appropriate in the case of a flexible duct, and if so, this method may provide a way to quantify the error in making that assumption.

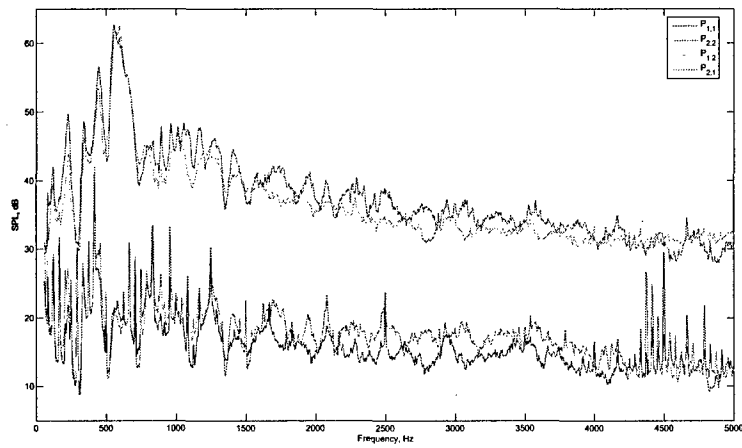


Figure A.2. Four combinations of two sound sources and two transfer functions.

APPENDIX B

Nomenclature

B	Number of blades
BPF	Blade passing frequency ($B\Omega$)
c	Speed of sound
C	Rotor blade chord
D	Dipole sound source in logarithmic scale
f	Frequency, Hz
G	Blocked acoustic transfer function in logarithmic scale
$G(\mathbf{r}, \mathbf{r}_0, f)$	True complex Green's function
He	Helmholtz number $\left(\frac{fD}{c_0}\right)$
k	Acoustic wave number $\left(\frac{\omega}{c}\right)$
L	Duct length
p_{ref}	Reference pressure, 20 mPa
\tilde{p}	Fourier transform of unsteady pressure
\mathcal{P}	Spectral density of unsteady pressure
Δp	Pressure rise across rotor
\vec{r}	Radial coordinate
\mathbf{r}	Far field observer location
\mathbf{r}_0	Far field observer location
R_{tip}	Rotor tip radius
R_d	Duct radius
SR	Speed Ratio $\left(\frac{\Omega_{max}}{\Omega_{min}}\right)$
St	Strouhal number $\left(\frac{2\pi R_t f}{V_{tip} B} = f/\text{BPF}\right)$
\tilde{u}	RMS of axial velocity
\bar{u}	Time mean axial velocity
U_0	Spatial mean axial velocity inside duct
U_{tip}	Relative fluid velocity at rotor tip $\left(\sqrt{(1 + \phi^2)}V_{tip}\right)$
V_{tip}	Rotor tip velocity ($R_t\Omega$)
\vec{x}	Axial coordinate
ρ	Fluid density
$\bar{\theta}$	Azimuthal coordinate
λ	Acoustic wavelength c/f

- ϕ Flow coefficient $\left(\frac{U_0}{U_{tip}}\right)$
 ψ Blade loading coefficient $\left(\frac{\Delta p}{1/2\rho U_{tip}^2}\right)$
 Ω Rotor rotation angular velocity $\left(\frac{V_{tip}}{2\pi R_t}\right)$

BIBLIOGRAPHY

- [1] M. E. Goldstein. *Aeroacoustics*. McGraw-Hill, 1976.
- [2] W. K. Blake. *Mechanics of Flow-induced Sound and Vibration, (two volumes)*. Academic Press Inc., 1986.
- [3] D. B. Stephens and S. C. Morris. A method for quantifying the acoustic transfer function of a ducted rotor. Submitted to the *Journal of Sound and Vibration*. *Under Review*, 2006.
- [4] D. B. Stephens and S. C. Morris. The effect of blade loading on sound sources in a ducted rotor. *12th AIAA/CEAS Aeroacoustics Conference*, 2006.
- [5] C. L. Morfey. The acoustics of axial flow machines. *Journal of Sound and Vibration*, 22(4):445-466, 1972.
- [6] P. E. Doak. Excitation, transmission and radiation of sound from source distributions in hard-walled ducts of finite length (i): The effects of duct cross-section geometry and source distribution space-time pattern. *Journal of Sound and Vibration*, 31(1):1-72, 1973.
- [7] D. L. Huff. Fan noise prediction: Status and needs. *NASA/TM-97-206533*, 1998.
- [8] H. Kobayashi. Three dimensional effects on pure tone fan noise due to inflow distortion. *AIAA 11th Fluid and Plasma Dynamics Conference*, 1978.
- [9] H. Kobayashi and J. F. Groeneweg. Effects of inflow distortion profiles on fan tone noise. *AIAA Journal*, 18(8):899-906, 1980.
- [10] H. M. Atassi, J. Fang, and S. Patrick. Direct calculation of sound radiated from bodies in nonuniform flows. *Journal of Fluids Engineering*, 115:573-579, 1993.
- [11] B. Elhadidi and H. M. Atassi. Passive control for turbofan tonal noise. *AIAA Journal*, 42(11):2279-2292, 2005.
- [12] W. Sears. Some aspects of non-stationary airfoil theory. *Journal of Aeronautical Science*, 8:104-108, 1941.
- [13] D. A. Lynch, W. K. Blake, and T. J. Mueller. Turbulence correlation length-scale relationships for the prediction of aeroacoustic response. *AIAA Journal*, 43(6):1187-1197, 2005.
- [14] D. F. Scharpf and T. J. Mueller. An experimental investigation of the sources of propeller noise due to the ingestion of turbulence at low-speeds. *Experiments in Fluids*, 18(4):227-287, 1995.

- [15] S. Subraminian. *Experimental and Computational Studies on Propeller Noise Due to Inflow Distortion*. PhD thesis, University of Notre Dame, 1993.
- [16] J. Wojno. *An Experimental Investigation of the Aeroacoustic Response of a Ted-Bladed Rotor Ingesting Grid-Generated Turbulence*. PhD thesis, University of Notre Dame, 1999.
- [17] R. Trunzo, B. Lakshminarayana, and D. E. Thompson. Nature of inlet turbulence and strut flow disturbances and their effect on turbomachinery rotor noise. *Journal of Sound and Vibration*, 76(2):233-259, 1981.
- [18] N. Moissev, B. Lakshminarayana, and D. E. Thompson. Noise due to interaction of boundary-layer turbulence with a compressor rotor. *Journal of Aircraft*, 15(1):53-61, 1978.
- [19] T. F. Brooks and M. A. Marcolini. Scaling of airfoil self-noise using measured flow parameters. *AIAA Journal*, 23(2):207-213, 1985.
- [20] T. F. Brooks, D. S. Pope, and M. A. Marcolini. Airfoil self-noise and prediction. *NASA-RP-1218*, 1989.
- [21] S. A. L. Glegg and C. Jochault. Broadband self-noise from a ducted fan. *AIAA Journal*, 36(8):1387-1395, 1998.
- [22] R.C. Dunne and M. S. Howe. Wall-bounded blade-tip vortex interaction noise. *Journal of Sound and Vibration*, 202(5):605-618, 1997.
- [23] C. Lee, M. K. Chung, and Y. H. Kim. A prediction model for the vortex shedding noise from the wake of an airfoil or axial flow fan blades. *Journal of Sound and Vibration*, 164(2):327-336, 1993.
- [24] R. E. Longhouse. Noise mechanism separation and design considerations for low tip-speed, axial flow fans. *Journal of Sound and Vibration*, 48(4):461-474, 1976.
- [25] R. C. Mellin. Selection of minimum noise fans for a given pumping requirement. *Noise Control Engineering*, 4:35-44, 1975.
- [26] U. W. Ganz, P. D. Joppa, T. J. Patten, and D. F. Scharpf. Boeing 18-inch fan rig broadband noise test. *NASA CR-1998-208704*, 1998.
- [27] A. D. Pierce. *Acoustics: An introduction to Its Physical Principles and Applications*. McGraw-Hill, New York, 1981.
- [28] H. Levine and J. Schwinger. On the radiation of sound from an unflanged circular pipe. *Physical Review*, 73(4):383-406, 1948.
- [29] M. Sevik. Sound radiation from a subsonic rotor subjected to turbulence. *NASA SP*, 304(11):493-511, 1974.
- [30] L. Mongeau, D. E. Thompson, and D. K. McLaughlin. A method for characterizing aerodynamic sound sources in turbomachines. *Journal of Sound and Vibration*, 181(3):369-389, 1995.
- [31] P. J. Huber. *Robust Statistics*. Wiley, 1981.

- [32] M. B. Bragg, D. C. Heinrich, and F. A. Balow. Flow oscillation over an airfoil near stall. *AIAA Journal*, 34(1):199–201, 1995.
- [33] A. P. Broeren and M. B. Bragg. Spanwise variation in the unsteady stalling flowfields of two-dimensional airfoil models. *AIAA Journal*, 39(9):1641–1691, 2001.